PASJ: Publ. Astron. Soc. Japan **59**, 653–678, 2007 April 25

A Comprehensive Study of Short Bursts from SGR 1806−20 and SGR 1900+14 Detected by HETE-2

Yujin E. NAKAGAWA,[1] Atsumasa YOSHIDA,[1,2] Kevin HURLEY,[3] Jean-Luc ATTEIA,[4]
Miki MAETOU,[1] Toru TAMAGAWA,[2] Motoko SUZUKI,[2] Tohru YAMAZAKI,[1]
Kaoru TANAKA,[1] Nobuyuki KAWAI,[2,5] Yuji SHIRASAKI,[2,6] Alexandre PELANGEON,[4]
Masaru MATSUOKA,[7] Roland VANDERSPEK,[8] Geoff B. CREW,[8] Joel S. VILLASENOR,[8]
Rie SATO,[5] Satoshi SUGITA,[1] Jun'ichi KOTOKU,[5] Makoto ARIMOTO,[5]
Graziella PIZZICHINI,[9] John P. DOTY,[8,10] and George R. RICKER[8]

[1]*Graduate School of Science and Engineering, Aoyama Gakuin University, 5-10-1 Fuchinobe, Sagamihara, Kanagawa 229-8558*
yujin@phys.aoyama.ac.jp
[2]*The Institute of Physical and Chemical Research, 2-1 Hirosawa, Wako, Saitama 351-0198*
[3]*Space Sciences Laboratory, University of California at Berkeley, 7 Gauss Way, Berkeley, CA 94720-7450, USA*
[4]*LATT, Observatoire Midi-Pyrénées, UMR5572, CNRS-UPS, 14 av. E.Belin, 31400 Toulouse, France*
[5]*Department of Physics, Tokyo Institute of Technology, 2-12-1 Ookayama, Meguro-ku, Tokyo, 152-8551*
[6]*National Astronomical Observatory of Japan, 2-21-1 Osawa, Mitaka, Tokyo 181-8588*
[7]*Tsukuba Space Center, JAXA, 2-1-1 Sengen, Tsukuba, Ibaraki 305-8505*
[8]*Center for Space Research, MIT, 70 Vassar Street, Cambridge, Massachusetts 02139, USA*
[9]*INAF/IASF Bologna, Via Gobetti 101, 40129 Bologna, Italy*
[10]*Noqsi Aerospace, Ltd., 2822 South Nova Road, Pine, Colorado 80470, USA*

(Received 2007 January 23; accepted 2007 March 8)

Abstract

Temporal and spectral studies of short bursts ($\lesssim$ a few hundred milliseconds) are presented for the soft gamma repeaters (SGRs) 1806−20 and 1900+14 using the HETE-2 samples. In five years from 2001 to 2005, HETE-2 localized 50 bursts from SGR 1806−20 and 5 bursts from SGR 1900+14. The cumulative number–intensity distribution of SGR 1806−20 in the active year 2004 is well described by a power-law model with an index of -1.1 ± 0.6. It is consistent with previous studies, but burst data taken in other years clearly give a steeper distribution. This may suggest that more energetic bursts could occur more frequently in periods of greater activity. From the data, the spectral evolution during bursts with a time scale of $\gtrsim 20$ ms does not seem to be common in the HETE-2 sample. The spectra of all short bursts are well reproduced by a two blackbody function with temperatures of ~ 4 and ~ 11 keV. From a timing analysis to the SGR 1806−20 data, a time lag of 2.2 ± 0.4 ms is found between the 30–100 keV and 2–10 keV radiation bands. This may imply (1) a very rapid spectral softening and energy reinjection, (2) diffused (elongated) emission plasma along the magnetic field lines in pseudo-equilibrium with multi-temperatures, or (3) a separate (located at $\lesssim 700$ km) emission region of a softer component (say, ~ 4 keV), which could be reprocessed X-rays by higher energy ($\gtrsim 11$ keV) photons from an emission region near the stellar surface.

Key words: gamma rays: observations — stars: pulsars: individual(SGR 1806−20, SGR 1900+14) — X-rays: stars

1. Introduction

The soft gamma repeaters (SGRs) are sources of repeating short-duration (~ 100 ms), soft-spectrum (below ~ 100 keV) bursts. Their activity periods are sporadic and unpredictable, and are punctuated by long periods of inactivity. More rarely, the SGRs emit giant flares that last for minutes and display very hard X- and gamma-ray spectra, extending into the MeV range. The first burst from a soft gamma repeater (SGR) was detected on 1979 January 7 by experiments on the Venera 11, ICE, and Prognoz-7 spacecraft (Mazets et al. 1981; Laros et al. 1986). This event was localized to a small region in the constellation Sagittarius, and was accordingly named SGR 1806−20. In the following months, a second SGR 1900+14 was discovered (Mazets et al. 1981). Around the same time, the first SGR giant flare occurred, on 1979 March 5 (Mazets et al. 1979; Cline et al. 1980; Evans et al. 1980; Fenimore et al. 1996) and was localized to a supernova remnant in the Large Magellanic Cloud. That source is currently known as SGR 0526−66.

For many years, little was known about the SGRs. The giant flares were initially thought to be a special class of gamma-ray bursts (GRBs) (Mazets et al. 1981), but since the SGRs emitted small bursts repeatedly, they eventually came to be recognized as a separate phenomenon. In the 1990's, quiescent soft X-ray observations ($\sim$ 1–10 keV) revealed that the SGRs were quiescent, periodic soft X-ray emitters. Their periods are on the order of seconds, and they display rapid spin-down rates (Kouveliotou et al. 1998). Furthermore, since some of the SGRs appeared to be associated with supernova remnants, they were regarded as a kind of X-ray pulsar. [Today,

these SNR–SGR associations have been questioned (Gaensler et al. 2001), and some indeed appear to be chance alignments, while other associations may be real.]

Ordinarily, isolated radio pulsars are thought to convert their rotational energy to radiation. In contrast, the energy released in the persistent X-ray emission from SGRs is too high to be explained in this way. In addition, there seem to be no fluctuations during their rotational periods, nor any sign of a companion star, so that SGRs cannot be accreting neutron stars, like the binary X-ray pulsars. Rather, the SGRs are thought to be magnetars, i.e., neutron stars with super-strong magnetic fields, (Duncan & Thompson 1992; Paczyński 1992; Thompson & Duncan 1995, 1996). Assuming that most of the spin-down energy loss is due to dipole radiation, the magnetic field strength should be $\sim 10^{15}$ G.

In the magnetar model, the surface of the neutron star is heated and fractured by the movement and dissipation of the magnetic field. The footpoints of the frozen-in magnetic field suddenly shift when a fracture occurs. This generates Alfvén waves that accelerate electrons, which in turn radiate their energy in short bursts. The giant flares are explained by global crustal fractures, which lead to magnetic reconnection, and energization of the neutron star magnetosphere, whose intense magnetic field contains the radiating electron–positron pair plasma (Thompson & Duncan 1995, 1996). The other models propose that bursting activity results from heating of the corona by magnetic reconnection (Lyutikov 2003), or glitches in the p-stars (Cea 2006).

Today, we know of four SGRs (1806−20, 1900+14, 0525−66, and 1627−41), as well as three candidates: SGR 1801−23 which emitted two bursts detected by BATSE and the Interplanetary Network in 1997 (Cline et al. 2000), SGR 1808−20 which emitted one burst detected by HETE-2 (the High Energy Transient Explorer) in 2003 (Lamb et al. 2003) and GRB/SGR 050925, which was detected by Swift (Holland et al. 2005). Compared with other bursting sources in our galaxy, such as type I and type II X-ray bursters, black hole X-ray transients, cataclysmic variables, and novae, SGR bursts are the brightest. Over the last $\sim$ 15 years, SGR 1806−20 and SGR 1900+14 have been the most active, with $\sim$ 500 and $\sim$ 175 short bursts observed, as well as one giant flare each.

Although the distances to SGR 1806–20 and SGR 1900+14 have been inferred by various methods, they still remain very uncertain. It was suggested earlier that the distance of SGR 1806−20 is $d = 15.0$ kpc, based on observations of molecular clouds along the line of sight (Corbel et al. 1997). A more recent study by Corbel and Eikenberry (2004) proposed $d = 15.0^{+1.8}_{-1.3}$ kpc based on millimeter and infrared observations along G10.0−0.3. Based on the measurements performed by observing the radio afterglow of the giant flare on 2004 December 27, two other estimates have been published. Cameron et al. (2005) suggest that its distance is between 6.4 kpc and 9.8 kpc, while McClure-Griffiths and Gaensler (2005) simply infer a lower limit of 6 kpc, and discuss that the most probable distance could be $d \sim 15$ kpc. If SGR 1900+14 is associated with G42.8+0.6, the distance is $\sim$ 5 kpc (Hurley et al. 1999). Alternatively, Vrba et al. (2000) found a compact cluster of massive stars near SGR 1900+14, suggesting that the distance was between 12 kpc and 15 kpc if this was its birthplace. In this paper, we assume distances of $d = 15$ kpc for SGR 1806−20 and $d = 10$ kpc for SGR 1900+14.

The absorbing neutral hydrogen column densities along the lines of sight towards SGR 1806−20 and SGR 1900+14 were investigated using ASCA data. They turned out to be $\sim 6 \times 10^{22}$ cm^{-2} for SGR 1806−20 (Sonobe et al. 1994) and $\sim 2 \times 10^{22}$ cm^{-2} for SGR 1900+14 (Hurley et al. 1999). The galactic values in the directions of the sources are roughly $\sim 1.53 \times 10^{22}$ cm^{-2} for SGR 1806−20, which is marginally consistent with the ASCA result, and $\sim 1.57 \times 10^{22}$ cm^{-2} for SGR 1900+14, which is fully consistent with the ASCA result (Dickey & Lockman 1990).

In some studies, the spectra of the short SGR bursts have been well fitted by an optically thin thermal bremsstrahlung (OTTB) spectrum (e.g., Aptekar et al. 2001). However, Laros et al. (1986) and Fenimore, Laros, and Ulmer (1994) reported that the spectra of bursts from SGR 1806−20 detected by ICE were not well described by OTTB or other simple models. Olive et al. (2004) reported that the spectra of an intermediate flare (i.e., several seconds long) from SGR 1900+14 detected by HETE-2 was not described by OTTB at lower energies (below 15 keV), but that they were best described by a two blackbody function (2BB). Similar results were reported for the short bursts from SGR 1900+14 (Feroci et al. 2004) and SGR 1806−20 (Nakagawa et al. 2005). Götz et al. (2006) reported that the spectrum of the large outburst from SGR 1806−20 was well fitted by OTTB, and they also noted the possibility of 2BB. Feroci et al. (2004) found that fits to the short bursts from SGR 1900+14 by a power law with an exponential cutoff gave acceptable results.

Some authors reported that there was weak or no spectral evolution for SGR bursts (Kouveliotou et al. 1987; Fenimore et al. 1994). In other observations, however, spectral softening during short bursts was reported from SGR 1806−20 (Strohmayer & Ibrahim 1998), in a $\sim$ 3.5 s long burst from SGR 1900+14 (Ibrahim et al. 2001), and in a $\sim$ 9 s long burst from SGR 0526−66 (Golenetskii et al. 1987). Furthermore, significant spectral evolution was reported for the weaker bursts from SGR 1806−20 (Götz et al. 2004, 2006).

Here, we report on the results of the temporal and spectral analyses of the short bursts from SGR 1806−20 and SGR 1900+14, whose durations are less than a few hundreds of milliseconds, using the data of the Wide-Field X-ray Monitor (WXM, 2–25 keV energy band: Shirasaki et al. 2003) and French Gamma Telescope (FREGATE, 6–400 keV energy band: Atteia et al. 2003) instruments on-board HETE-2. We discuss the spectral evolution, the emitting region, the cumulative number–intensity distribution, and the spectral modeling of the short bursts, and confront our results with theoretical models.

2. Observations

The primary purpose of HETE-2 is to investigate cosmic high-energy transient phenomena, such as GRBs (Ricker et al. 2003). The scientific instruments on-board HETE-2 always point in the anti-solar direction; the galactic center region comes into the field of view during the summer season; at that time bursts from SGR 1806−20

Table 1. Number of the events and bursts analysed.*

Year	SGR 1806−20			SGR 1900+14			Nonlocalized events
	Localized events	Bursts		Localized events	Bursts		
2001	2	1	(1)	5	4	(4)	5
2002	0	0	(0)	1	1	(1)	5
2003	9	8	(8)	0	0	(0)	12
2004	40	33	(32)	0	0	(0)	87
2005	11	8	(8)	0	0	(0)	4
Total	62	50	(49)	6	5	(5)	113

* The left column ("Localized events") for each SGR shows the number of localized events. The right columns ("Bursts") are the number of bursts which we employ in our analyses for each SGR. Since one event contains two bursts in the case of #2800, the number of events which we employ in our analyses is indicated in parentheses. The last ("Nonlocalized events") shows the number of nonlocalized events.

and SGR 1900+14 are best observed.

Most of the bursts from the SGRs trigger the instruments in the 6–80 keV or 30–400 keV energy range, on a 20 ms time scale, while some bursts trigger them in the 2–25 keV energy range on a 320 ms time scale. Based on these criteria, HETE-2 triggered on 181 events in the summer periods from 2001 June 18, through 2005 August 7. We localized these events using data from the WXM, and found that 62 were from SGR 1806−20 and 6 were from SGR 1900+14, while 113 events were out of the WXM field of view ($> 35°$ off axis) or too weak to be localized ($< 10^{-7}$ erg cm^{-2}). Table 1 contains more details. Although these nonlocalized events were presumably bursts from SGR 1806−20 or SGR 1900+14 considering the field-of-view of the instruments and their short durations ($\lesssim$ a few $\times$100 ms) we do not include them in the current analyses.

In this paper, we call *events* the set of data recorded after triggers by the instruments on the spacecraft. Some events contain a single burst, and others are better described as containing several separate bursts (see below). The localized events include two intermediate flares (HETE-2 trigger numbers #1576 and #3800), which we exclude from our analysis. We also exclude the following events: HETE-2 trigger #1560, a burst from SGR 1806−20, in which the time-tagged photon data from the WXM were lost, three events in which the FREGATE time-tagged photon data were lost (#3290, #3801, and #3845), five events for which the downlinked tagged times were out of order (#2768, #2810, #3282, #3404, and #3418), and three events whose data were corrupted due to strong X-ray sources like Sco-X1 in the field-of-view, which made detailed analysis very difficult (#3273, #3274, and #3349). Therefore we retain 49 events containing 50 bursts from SGR 1806−20, and 5 events containing 5 bursts from SGR 1900+14.

To compare HETE-2 results with previous studies, event classification is done using methods similar to those in Göğüş et al. (2001). The events are classified into single-peaked bursts and multiple-peaked bursts using light curves with 5 ms binning. Examples are given in figure 10 (p.674) for the single-peaked bursts and in figure 8 (p.662) for the multiple-peaked bursts. 22 out of 50 bursts from SGR 1806−20 are single peaked and 28 are multiple peaked. From

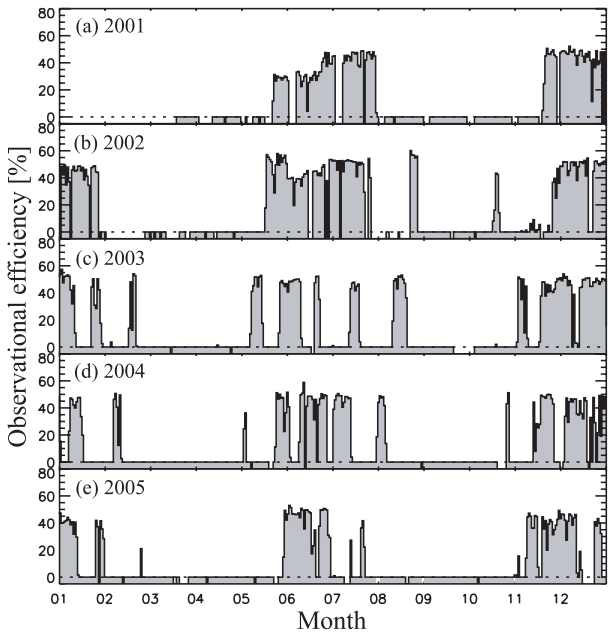

Fig. 1. Time history of the observational efficiency for each day (UT) of the WXM for SGR 1806−20. The blank regions without hatching represent periods in which aspect or housekeeping data were lost (e.g., because of a downlink problem).

SGR 1900+14, four-single peaked and one multiple-peaked bursts were detected. For the multiple-peaked bursts, if the interval between the first peak and the second peak is greater than T_{90} for the first peak (T_{90} is defined as the time to accumulate between 5% and 95% of the observed photons), the second peak is treated as another burst. If we find two bursts within one event, we distinguish those bursts using letters A and B. There are five triggered events that contain two bursts from SGR 1806−20 (#2800, #3347, #3365, #3368, and #3399); only one of them (#2800) gives a significant localization to SGR 1806−20 for each burst, and is included in the sample for the analyses. The number of localized events and bursts employed in our analyses are summarized in table 1. Note that SGR 1806−20 became very active in 2004, and 40 events triggered in the summer of 2004. In contrast,

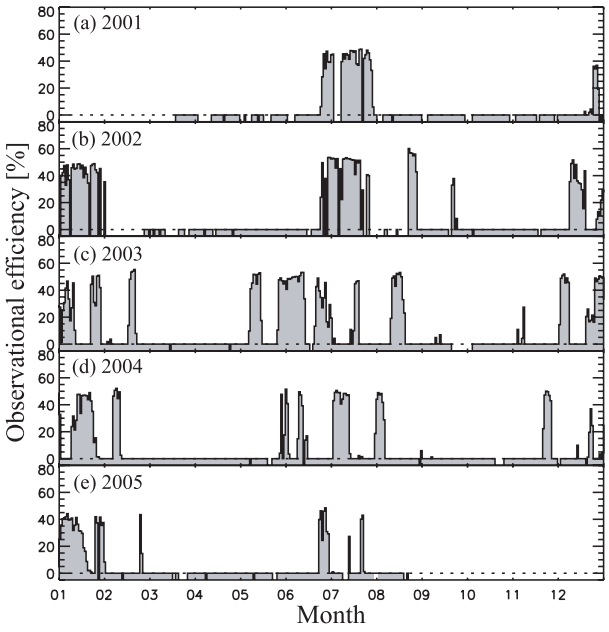

Fig. 2. Same plot as figure 1 for SGR 1900+14.

Table 2. Number of localized bursts.*

Year	SGR 1806−20		SGR 1900+14	
2001	7	(3290)	12	(1160)
2002	0	(5140)	2	(2820)
2003	27	(4390)	0	(3280)
2004	92	(3700)	0	(2090)
2005	21	(3100)	0	(1100)
Total	147	(19620)	14	(10450)

* It is corrected for the observational efficiency, by year and source. The observing durations are given in parentheses in units of kilosecond.

SGR 1900+14 has been in a relatively quiescent phase since HETE-2 launch. All of the analyzed bursts are listed in tables 3 and 4, in which the single-peaked bursts are indicated by *s* and the multiple-peaked ones by *m*.

The observational efficiencies were estimated for each source from 2001 June to 2005 August. First, we calculated the fraction of time when the high voltage was on ($\varepsilon_{\rm hv}$), since HETE-2 performs observations only during orbit night. Then we derived the fraction of the time when each SGR was in the field-of-view of the 35° WXM ($\varepsilon_{\rm fov}$). The observational efficiency is given by $\varepsilon_{\rm hv} \times \varepsilon_{\rm fov}$ for each source. The WXM on-board HETE-2 is operated so that the high voltage is turned off during the periods when the earth is in the field-of-view. Therefore $\varepsilon_{\rm hv}$ takes into account earth occultations.

Figure 1 and figure 2 show time histories of the observational efficiencies with one day resolution for SGR 1806−20 and SGR 1900+14, respectively. The blank regions without hatching represent periods in which aspect or housekeeping data were lost (e.g., because of a downlink problem).

With these observational efficiencies, the expected number of bursts was estimated for each year. Table 2 gives these numbers, as well as the observing time in kiloseconds.

3. Analysis

3.1. Temporal Analysis

3.1.1. Distribution of T_{90}

To study the burst durations, we calculated T_{90} for all the samples from SGR 1806−20 and SGR 1900+14. Our samples did not have any too-bright burst for which the dead time would need to be considered for analyses.

The T_{90} durations are given in tables 3 and 4. Figure 3 shows the relation between the T_{90} durations in the 6–30 keV and 30–100 keV energy ranges for the single-peaked bursts (left) and the multiple-peaked bursts (right); the dotted lines indicate equal T_{90} durations in both energy ranges. Outlying points indicate that the burst might have spectral evolution. The circles and squares show the T_{90} durations for SGR 1806−20 and SGR 1900+14, respectively. Although most of the bursts lie on the dotted lines (i.e., they appear to be consistent with no spectral evolution), we find that 13 single-peaked bursts from SGR 1806−20 (indicated by *b* in table 3) and one single-peaked burst from SGR 1900+14 (indicated by *b* in table 4) lie far from them. We also find that 10 multiple-peaked bursts from SGR 1806−20 (indicated by *c* in table 3) are significantly inconsistent with the dotted line.

We also studied the hardness ratios for the bursts from SGR 1806−20 and SGR 1900+14 as a function of time. The hardness ratio *HR* is defined by $HR = (H - S)/(H + S)$ where S is the 6–30 keV count rate and H is the 30–100 keV count rate. The hardness ratios are summarized in figure 4. We find that three short bursts (#3340, #3365A, and #3874, which are indicated by *d* in table 3) have clear spectral softening, while another three (#2800A, #3356, and #3370, which are indicated by *e* in table 3) might have a hard component at end of the burst. Although one short burst, #3348, seems to show a marginal spectral softening, the last three bins of its hardness ratios have large uncertainties. It is thus omitted from the above group.

As a control, we also calculated the hardness ratios for eight short bursts that clearly lie on the dotted lines (indicated by *a* in tables 3 and 4). These hardness ratios are shown in figure 5, and no spectral evolution is seen for them.

3.1.2. Time lag

Some bursts seem to display delayed soft emission (e.g., #3259—see figure 8 in p.662). To investigate systematically if a delay appears in the softer energy band, the time lag, $T_{\rm lag}$ between the 2–10 keV and 30–100 keV time histories, and between the 6–30 keV and 30–100 keV time histories, were evaluated by cross-correlating them. In our definition, the time lag has a positive value when the soft emission is delayed from the hard emission. Here, the boundary energy of 30 keV was chosen because it is approximately the dividing point between the spectral components in a two blackbody function (see subsubsection 3.2.3 and subsection 4.3).

In order to select statistically significant bursts for this analysis, we proceeded in the following way. First, background-subtracted light curves were generated with 5 ms time bins to select bursts using the peak count rates in the 2–10 keV, 6–30 keV, and 30–100 keV energy ranges. To estimate a correct peak count rate, the phasing of the time bins (i.e., the beginning time of $t = 0$ bin) is important. We

Table 3. Main properties of the short bursts from SGR 1806−20.

Trigger #*	Trigger date (UT)	T_{90}† duration (ms)			Total counts			Note‡
		2–25 keV	6–30 keV	30–100 keV	2–25 keV	6–30 keV	30–100 keV	
1566	2001:06:23.15:54:53	184± 6	192± 4	206±22	1020	2200	280	*c*, *l*, *m*
2770	2003:07:18.23:43:12	136±37	116± 13	196±42	363	660	125	*b*, *s*
2771	2003:07:19.03:24:15	268±17	358±103	366±62	276	617	119	*s*
2773	2003:07:19.22:34:15	196±29	188± 5	234±43	957	2870	534	*c*, *l*, *s*
2800A	2003:08:11.16:06:28	72±21	68± 8	106±40	441	1070	180	*b*, *e*, *l*, *s*
2800B	2003:08:11.16:06:28	160±27	172± 15	198±29	254	461	86	*b*, *s*
2802	2003:08:13.09:52:03	146±11	146± 6	136±11	809	2020	2020	*h*, *l*, *m*
2806	2003:08:15.11:15:24	98±28	96± 40	84±19	126	293	194	*h*, *s*
2812	2003:08:18.23:16:01	180±18	152± 29	176± 8	445	1160	721	*c*, *h*, *m*
3259	2004:05:28.22:13:55	466± 5	458± 2	464±15	1490	6310	766	*a*, *l*, *m*
3291	2004:05:31.14:20:00	48±23	26± 10	34±21	222	527	74	*a*, *l*, *s*
3303	2004:06:02.09:42:02	568± 8	572± 6	582±14	1920	3910	684	*a*, *l*, *m*
3305	2004:06:02.16:00:01	146±14	142± 3	148±17	333	609	112	*m*
3326	2004:06:10.18:26:22	326±14	324± 14	358±24	1170	2550	377	*c*, *m*
3329	2004:06:11.00:49:23	184±36	192± 6	222±40	152	344	81	*m*
3331	2004:06:11.03:44:45	206±19	218± 12	246±62	544	1310	199	*m*
3340	2004:06:15.12:00:42	116±20	94± 17	132±22	367	737	469	*b*, *d*, *h*, *s*
3343	2004:06:15.16:53:56	134±42	100± 16	174±31	134	255	173	*b*, *h*, *s*
3344	2004:06:15.23:17:03	100±24	122± 45	142±35	112	291	144	*h*, *s*
3346	2004:06:16.21:27:28	178±33	200± 26	250±27	168	436	221	*b*, *h*, *s*
3347A	2004:06:16.21:40:07	130± 9	140± 37	134±14	329	603	401	*h*, *s*
3348	2004:06:16.23:15:44	84±30	96± 12	44± 5	447	954	796	*b*, *h*, *s*
3350	2004:06:17.00:50:34	114±35	104± 6	134±20	206	368	192	*c*, *h*, *m*
3351	2004:06:17.13:26:12	126±17	116± 9	108±21	1340	4700	963	*l*, *m*
3352	2004:06:17.17:14:37	88±11	64± 8	234±64	262	573	85	*b*, *s*
3355	2004:06:18.17:01:37	36± 7	38± 15	56±23	147	430	69	*s*
3356	2004:06:19.00:50:02	64±17	52± 4	62±10	371	917	168	*b*, *e*, *l*, *s*
3359	2004:06:20.21:49:27	68±20	64± 12	68±34	489	1730	423	*l*, *s*
3363	2004:06:22.07:34:47	218±75	220± 35	414±75	357	936	187	*c*, *m*
3365A	2004:06:23.15:30:58	64±23	46± 12	30± 9	258	736	138	*b*, *d*, *s*
3368B	2004:06:23.22:16:37	140± 8	126± 5	130±22	1520	5250	1100	*l*, *s*
3369	2004:06:23.22:20:50	272± 8	264± 9	284±53	901	2150	353	*l*, *m*
3370	2004:06:23.23:43:30	456±46	360± 10	462±27	551	1180	211	*c*, *e*, *m*
3372	2004:06:24.05:51:05	128±26	124± 9	168±77	301	676	141	*m*
3375	2004:06:25.07:45:03	160±23	148± 23	282±61	336	902	160	*c*, *m*
3378	2004:06:25.13:51:57	60±10	98± 14	108±40	149	433	74	*s*
3387	2004:06:27.09:15:41	74± 5	72± 6	76±10	725	2810	569	*a*, *l*, *m*
3388	2004:06:27.17:29:37	80±35	76± 19	58±21	148	490	54	*s*
3399A	2004:07:06.11:29:57	176±14	156± 8	210±23	512	1210	183	*b*, *l*, *s*
3403	2004:07:08.00:38:10	254±29	234± 33	240±71	198	331	96	*m*
3405	2004:07:08.06:45:09	48±23	54± 10	54±25	283	854	137	*a*, *l*, *s*
3412	2004:07:11.03:59:04	208±12	220± 18	194±21	390	974	176	*c*, *m*
3846	2005:06:25.21:48:06	108± 9	94± 6	92±22	101	296	119	*a*, *s*
3847	2005:06:26.16:53:13	128±11	132± 7	136±15	304	574	150	*s*
3848	2005:06:26.18:24:18	158±21	164± 24	142±22	731	1610	449	*b*, *h*, *l*, *s*
3851	2005:06:27.18:31:30	58±40	100± 5	108±16	196	505	75	*m*
3852	2005:06:27.20:10:49	128±13	136± 11	118±11	408	879	116	*b*, *s*
3854	2005:06:28.05:49:29	52±24	60± 11	70±21	273	564	52	*s*
3873	2005:07:22.14:43:32	110±20	108± 3	106±23	457	954	129	*m*
3874	2005:07:22.14:55:15	156±10	146± 6	160± 8	1340	3680	496	*c*, *d*, *m*

∗ HETE-2 trigger number.

† T_{90} is the time to accumulate between 5% and 95% of the counts.

‡ Note for each burst; *a* denotes a burst lying on the dotted lines described in figure 3 for which we calculated the hardness ratio, *b* denotes single peaked bursts lying off the dotted line described in figure 3, *c* denotes multiple peaked bursts lying off the dotted line described in figure 3, *d* denotes bursts which have clear spectral softening, *e* denotes bursts which have a hard component later in the burst, *h* denotes bursts observed with the high gain configuration, *l* denotes bursts which we employed to estimate $T_{\rm lag}$, *s* denotes single peaked bursts, and *m* denotes multiple peaked bursts.

Table 4. Main properties of the short bursts from SGR 1900+14.

Trigger #*	Trigger date (UT)	T_{90}† duration (ms)			Total counts			Note‡
		2–25 keV	6–30 keV	30–100 keV	2–25 keV	6–30 keV	30–100 keV	
1568	2001:06:27.23:24:18	94± 7	132±31	144±34	151	938	153	*m*
1571	2001:06:28.15:06:36	300±27	294±12	300±34	673	4520	754	*a*, *m*
1572	2001:06:29.12:13:32	98± 8	104±25	100± 8	98.9	692	106	*a*, *s*
1578	2001:07:03.06:55:04	118±27	130± 5	130±30	145	783	114	*s*
2310	2002:08:27.15:35:15	84±18	86±26	60±13	126	217	42	*b*, *s*

* HETE-2 trigger number.
† T_{90} is the time to accumulate between 5% and 95% of the counts.
‡ Note for each burst; *a* denotes a burst lying on the dotted lines described in figure 3 for which we calculated the hardness ratio, *b* denotes single peaked bursts lying off the dotted line described in figure 3, *s* denotes single peaked bursts, and *m* denotes multiple peaked bursts.

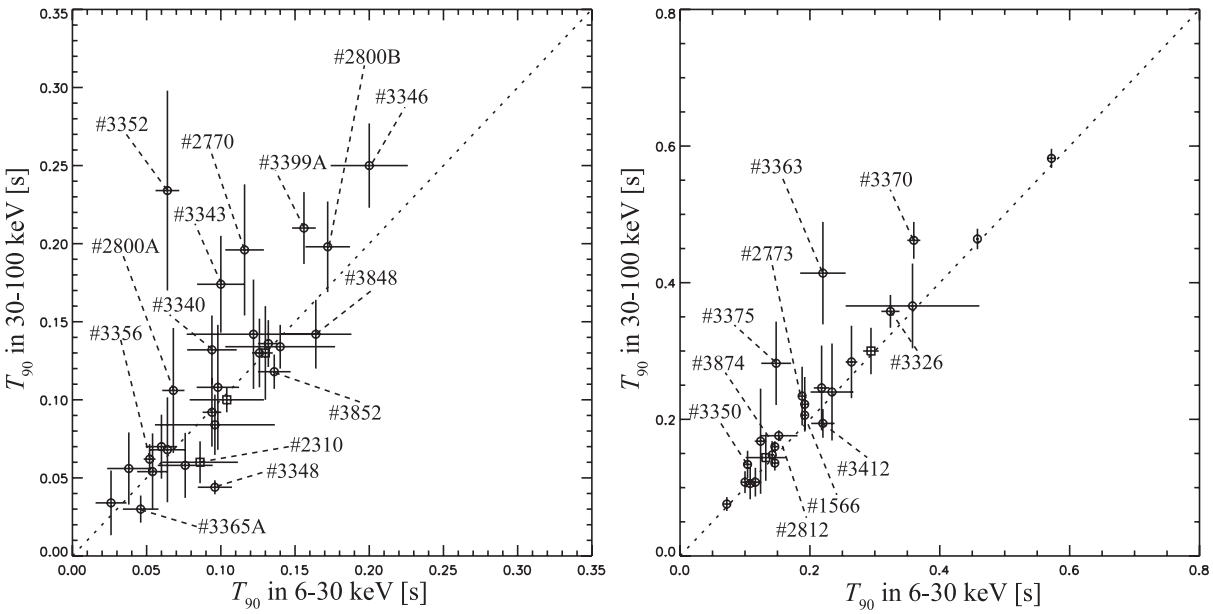

Fig. 3. Distribution of T_{90} durations for the single peaked bursts (left) and multiple peaked bursts (right). The circle and square show the T_{90} durations for SGR 1806−20 and SGR 1900+14, respectively. The dotted lines indicate equal 6–30 keV and 30–100 keV T_{90}'s. The quoted errors are for 90% confidence.

determined the phase by shifting a beginning time of $t = 0$ bin with a 0.25 ms time interval so that the peak count rate in the light curve obtained the maximum value. Using this method, the 5 ms light curves and peak count rates were derived. The cross-correlation coefficients were calculated for each burst. We searched the requirements of the peak count rate by investigating whether the peak of the cross-correlation coefficients was clearly seen or not for each burst. As a result, we required the peak count rates to be $> 10\sigma_1$, $> 20\sigma_2$, and $> 22\sigma_3$ in the 2–10 keV, 6–30 keV, and 30–100 keV energy ranges, respectively, where $\sigma_1 = 0.4$, $\sigma_2 = 0.6$, and $\sigma_3 = 0.2$ counts ms^{-1} are the standard deviations of the background in each band. We did not employ bursts showing clear spectral softening (#3340, #3365A, and #3874), and omitted any burst with a marginal spectral softening (#3348) either to avoid affecting the time-lag analysis.

After these selections, only 16 bursts from SGR 1806−20 survived for the $T_{\rm lag}$ analysis, which are indicated by *l* in table 3. There were no bursts satisfying the above criteria for SGR 1900+14.

To calculate the cross-correlation coefficients, background-subtracted light curves with 0.2 ms time bins were generated for each burst (their phases were determined with a 0.01 ms time interval). We then smoothed the light curves to reduce fluctuations. The moving average, $N(t)'$, at a given time was calculated by $[N(t) + N(t - \Delta t)]/2$, where t is the time, Δt is the time resolution of the light curve and $N(t)$ and $N(t - \Delta t)$ are the count rates. Even after this smoothing, however, the cross-correlation coefficients still displayed large fluctuations. We therefore made an ensemble average by assuming that all of the bursts were samples from the same parent population; in other words, the same physical process controls the radiation for all short bursts.

The resultant cross-correlation coefficients were fitted with a Gaussian model, a symmetric exponential component model, and a Lorentzian model, for all of which the time lag was

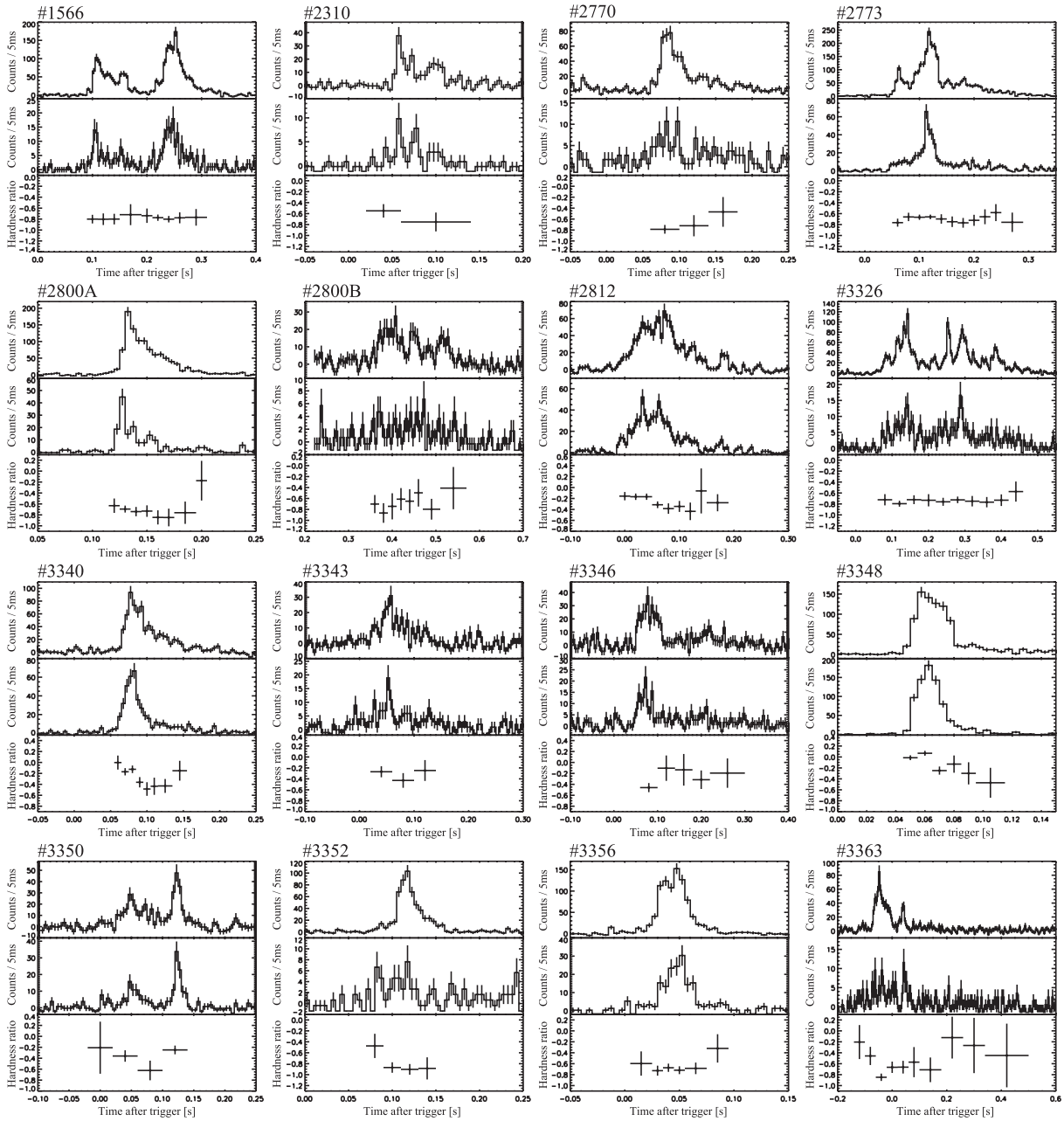

Fig. 4. Light curves observed by FREGATE in the 6–30 keV (top panels) and the 30–100 keV energy bands (middle panels), and time resolved hardness ratio (bottom panels) for all short bursts which do not lie on the dotted lines described in figure 3. The quoted errors are for 68% confidence.

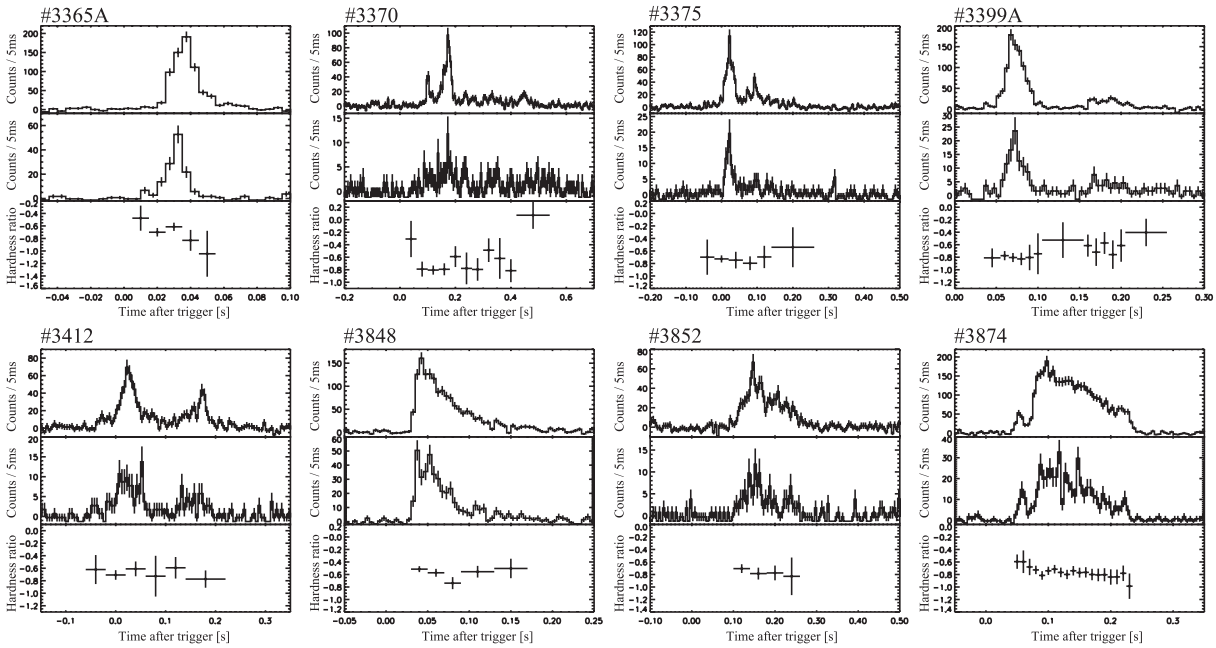

Fig. 4. (Continued.)

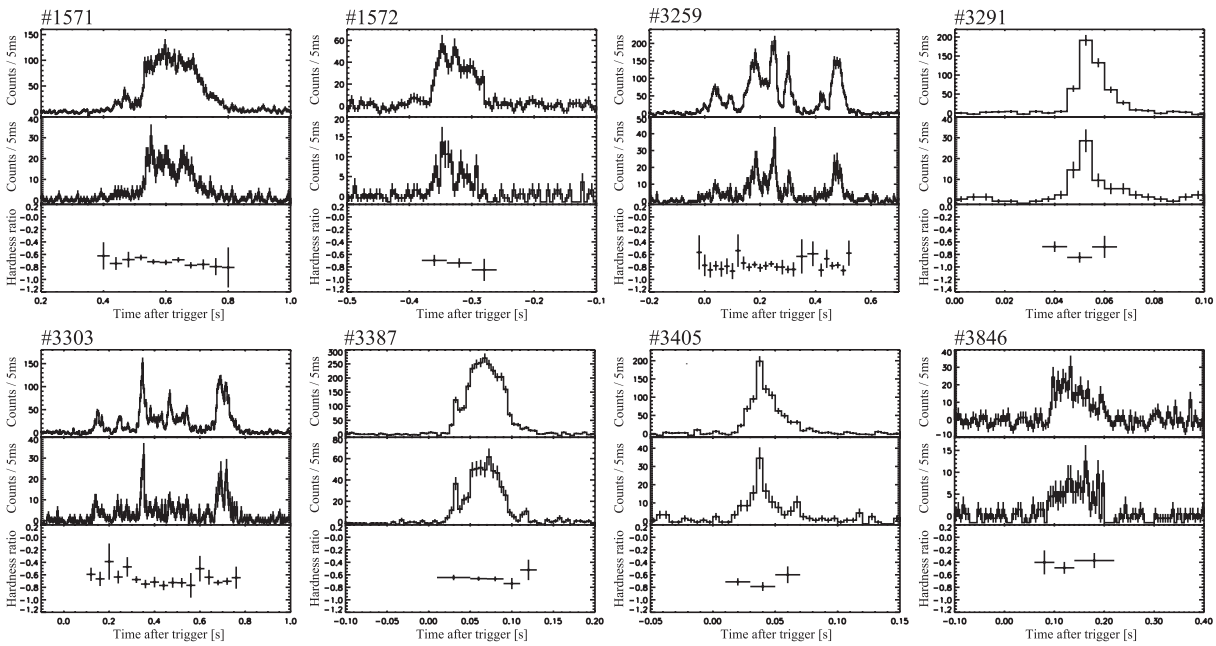

Fig. 5. Light curves observed by FREGATE in the 6–30 keV (top panels) and the 30–100 keV (middle panels) energy bands, and the time resolved hardness ratio (bottom panels); these are for the short bursts which lie on the dotted lines described in figure 3 (i.e., no spectral evolution). The quoted errors are for 68% confidence.

derived to be positive. Here, we employ the Lorentzian model because it best reproduces the shape of the cross-correlation coefficient. The best-fit $T_{\rm lag}$ is 2.2 ± 0.4 ms between the 2–10 keV and 30–100 keV time histories, and 1.2 ± 0.3 ms between 6–30 keV and 30–100 keV. Here, the quoted errors are the total uncertainties ($\sqrt{{\sigma_{\rm stat}}^2 + {\sigma_{\rm sys}}^2}$), considering the time resolutions of the light curves (0.2 ms) and the instruments [256 μs for the WXM (Shirasaki et al. 2003) and 6.4 μs for the FREGATE (Atteia et al. 2003)], and therefore systematic uncertainties ($\sigma_{\rm sys}$) of 0.3 ms and 0.2 ms for the time lag between the 2–10 keV and 30–100 keV bands, and between the 6–30 keV and 30–100 keV bands, respectively. Figure 6 shows the cross-correlation coefficients between 2–10 keV and 30–100 keV, and the typical 1σ error is presented in the figure.

For each of the 16 bursts, 100 light curves were simulated for both the 2–10 keV and 30–100 keV band to investigate if the

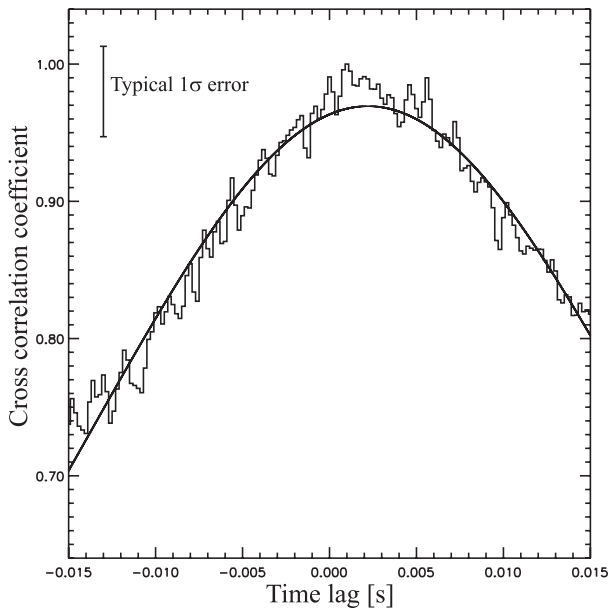

Fig. 6. Cross-correlation coefficients between the 2–10 keV and 30–100 keV time histories.

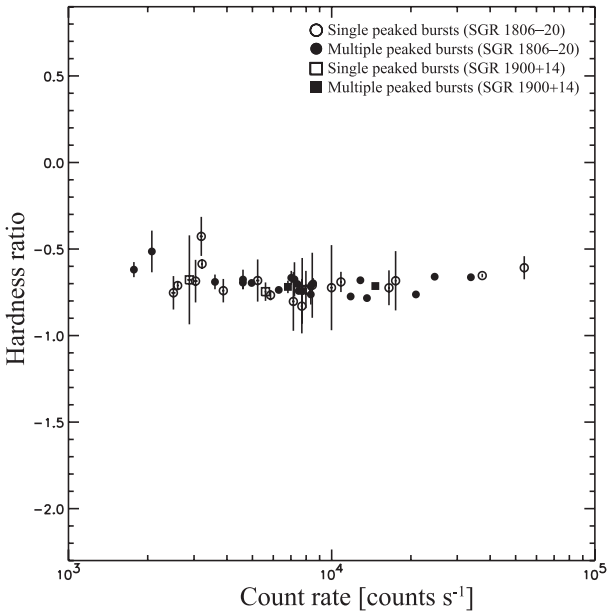

Fig. 7. Relation between the 6–100 keV count rate and the hardness ratio. 11 bursts observed with the different gain configuration (indicated by *h* in table 3) are not employed in this figure.

Table 5. Spectral parameters obtained using 2BB model for #3259.

Time region	$N_{\rm H}$*	$kT_{\rm LT}$†	$R_{\rm LT}\left(\frac{d}{15\,{\rm kpc}}\right)$‡	$kT_{\rm HT}$†	$R_{\rm HT}\left(\frac{d}{15\,{\rm kpc}}\right)$‡	$F_{\rm X}$§	F_γ§	χ^2 (d.o.f.)
(s)	(10^{22} cm^{-2})	(keV)	(km)	(keV)	(km)			
−0.010–0.065	< 49	$2.6^{+1.1}_{-0.9}$	63^{+147}_{-30}	$7.4^{+2.1}_{-1.2}$	$8.4^{+4.9}_{-3.9}$	39^{+16}_{-16}	128^{+32}_{-32}	22 (26)
0.065–0.120	< 23	$1.5^{+0.8}_{-0.7}$	97^{+168}_{-52}	$6.0^{+1.5}_{-1.1}$	$10.8^{+4.6}_{-4.5}$	...	...	22 (21)
0.120–0.215	11^{+12}_{-7}	$4.2^{+0.6}_{-0.8}$	46^{+16}_{-9}	$9.1^{+5.3}_{-2.2}$	$6.1^{+8.7}_{-4.4}$	65^{+8}_{-8}	348^{+89}_{-89}	41 (47)
0.215–0.275	< 9	$5.0^{+0.6}_{-3.4}$	39^{+65}_{-5}	$9.4^{+6.7}_{-3.5}$	$6.1^{+13.3}_{-4.9}$	85^{+10}_{-10}	499^{+173}_{-173}	43 (47)
0.275–0.395	26^{+46}_{-25}	$1.5^{+2.7}_{-0.5}$	158^{+336}_{-125}	$5.4^{+0.6}_{-0.3}$	$17.9^{+5.2}_{-5.7}$	30^{+17}_{-17}	109^{+21}_{-21}	22 (29)
0.395–0.440	< 32	$4.3^{+0.6}_{-0.7}$	27^{+18}_{-7}	> 10.4	$0.2^{+1.1}_{-0.1}$	28^{+7}_{-7}	135^{+48}_{-48}	10 (15)
0.440–0.520	< 9	$4.5^{+0.5}_{-0.8}$	41^{+6}_{-6}	$10.3^{+18.1}_{-3.2}$	$4.0^{+8.3}_{-3.5}$	71^{+8}_{-8}	342^{+101}_{-101}	35 (40)

* Photoelectric absorption with 90% confidence level uncertainties.
† Blackbody temperatures with 90% confidence level uncertainties.
‡ Emission radii with 90% confidence level uncertainties; d is the distance to the source. We have used $d = 15$ kpc.
§ X-ray (2–10 keV) and gamma-ray (10–100 keV) fluxes, 10^{-8} erg cm^{-2} s^{-1}, with 68% confidence level uncertainties.

derived lag is just due to fluctuations of the counts. Applying the same method for the observational data, time lags were found to be distributed above 0.6 ms (peaked at 1.5 ms) in these simulated data. Therefore, we conclude that the nonzero time lag is real.

Using the peak count rates derived above, the relation between the 6–100 keV fluence and the hardness ratio was also investigated (figure 7). 11 bursts observed with different gain configurations (indicated by *h* in table 3) are not employed in this figure. There seems to be no significant correlation. This result is consistent with previous studies (Fenimore et al. 1994; Götz et al. 2004, 2006).

3.2. *Spectral Analysis*

The following eight functions were used as models for spectral fitting of all the samples: 1) a power-law model (PL), 2) a power law with an exponential cutoff (PLE), 3) a single blackbody (BB), 4) a two-blackbody function (2BB), 5) a disk-blackbody model (disk-BB), 6) an optically thin thermal bremsstrahlung model (OTTB), 7) OTTB with the BB model (BB+OTTB), and 8) PL with the BB model (BB+PL).

If we add photoelectric absorption to the 2BB model, we find that the column densities are consistent with zero (i.e., no absorption). On the other hand, if we adopt the photoelectric absorptions derived from the ASCA observations of the quiescent emission (see section 1), we find unacceptable results

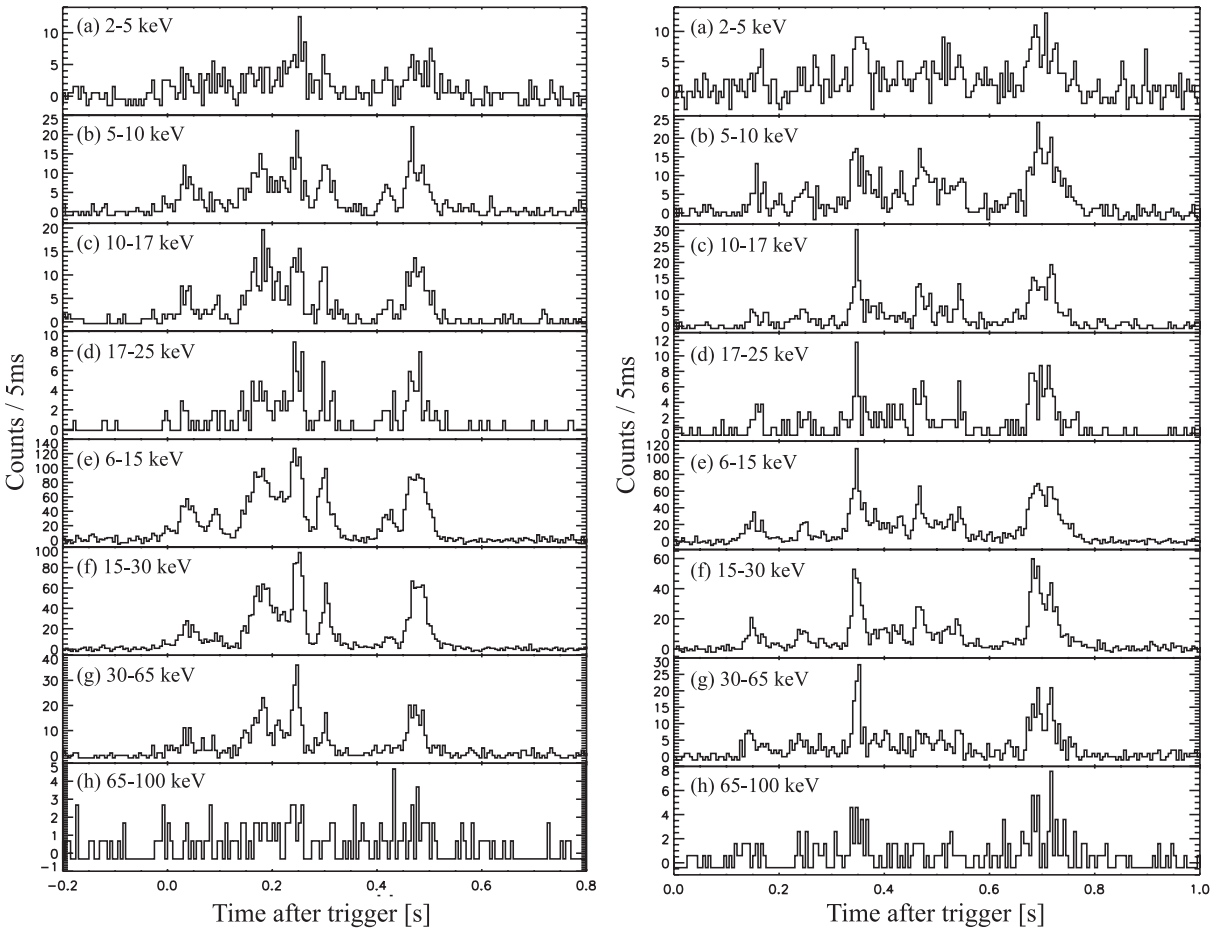

Fig. 8. Time history of #3259 (left) and #3303 (right) observed by the WXM in the energy bands 2–5 keV (a), 5–10 keV (b), 10–17 keV (c), and 17–25 keV (d), and by FREGATE in the 6–15 keV (e), 15–30 keV (f), 30–65 keV (g), and 65–100 keV (h) energy bands with 5 ms time bins.

Table 6. Spectral parameters obtained using 2BB model for #3303.

Time region	$N_{\rm H}$*	$kT_{\rm LT}$†	$R_{\rm LT}\left(\frac{d}{15\,{\rm kpc}}\right)$‡	$kT_{\rm HT}$†	$R_{\rm HT}\left(\frac{d}{15\,{\rm kpc}}\right)$‡	$F_{\rm X}$§	F_γ§	χ^2 (d.o.f.)
(s)	(10^{22} cm^{-2})	(keV)	(km)	(keV)	(km)			
0.130–0.215	< 54	$3.8^{+1.4}_{-2.0}$	19^{+13}_{-8}	$11.1^{+13.5}_{-4.1}$	$2.2^{+1.9}_{-1.8}$	12^{+10}_{-10}	60^{+38}_{-38}	13 (11)
0.215–0.330	< 37	$2.2^{+1.5}_{-1.0}$	49^{+180}_{-31}	$8.4^{+1.6}_{-1.4}$	$4.8^{+2.3}_{-1.7}$	13^{+9}_{-9}	59^{+16}_{-16}	28 (30)
0.330–0.450	< 9	$3.6^{+0.6}_{-1.1}$	36^{+21}_{-7}	$10.3^{+2.2}_{-1.7}$	$5.0^{+3.0}_{-2.0}$	41^{+51}_{-38}	200^{+1010}_{-172}	42 (39)
0.450–0.620	< 15	$3.9^{+0.7}_{-1.0}$	27^{+17}_{-6}	$9.1^{+3.8}_{-2.1}$	$4.3^{+4.4}_{-2.7}$	24^{+5}_{-5}	115^{+39}_{-39}	25 (34)
0.620–0.705	< 7	$4.4^{+0.5}_{-0.5}$	30^{+7}_{-5}	$15.0^{+6.3}_{-3.3}$	$2.1^{+1.5}_{-1.0}$	39^{+8}_{-8}	218^{+48}_{-48}	49 (48)
0.705–0.775	< 24	$5.0^{+0.7}_{-1.0}$	24^{+11}_{-5}	$12.3^{+14.3}_{-3.9}$	$2.7^{+4.7}_{-2.1}$	31^{+7}_{-7}	213^{+112}_{-112}	32 (35)

* Photoelectric absorption with 90% confidence level uncertainties.
† Blackbody temperatures with 90% confidence level uncertainties.
‡ Emission radii with 90% confidence level uncertainties; d is the distance to the source. We have used $d = 15$ kpc.
§ X-ray (2–10 keV) and gamma-ray (10–100 keV) fluxes, 10^{-8} erg cm^{-2} s^{-1}, with 68% confidence level uncertainties.

for a few cases. Considering these results, we performed spectral analyses using 2BB with a photoelectric absorption model in which the galactic absorptions were adopted as the lower limit values.

The single-component models (PL, BB, and OTTB) were rejected, while BB+OTTB, PLE, disk-BB, and BB+PL gave acceptable fits, with a few exceptions, and 2BB gave even better fits for all cases.

Because of the effects due to problems of intercalibration (the reason is under investigation), the FREGATE spectra

Table 7. Spectral parameters obtained using BB+OTTB model for SGR 1806−20.

Trigger #*	$N_{\rm H}$† (10^{22} cm^{-2})	$kT_{\rm BB}$‡ (keV)	$R_{\rm BB}\left(\frac{d}{15\,{\rm kpc}}\right)$§ (km)	$kT_{\rm OTTB}$‖ (keV)	$F_{\rm X}$#	F_γ#	χ^2 (d.o.f.)
1566	9^{+8}_{-6}	$5.1^{+0.9}_{-0.5}$	19^{+6}_{-8}	24^{+12}_{-6}	45^{+5}_{-5}	202^{+30}_{-30}	11 (34)
2770	<18	$4.0^{+0.5}_{-0.7}$	22^{+6}_{-7}	41^{+160}_{-19}	25^{+4}_{-4}	94^{+28}_{-28}	23 (32)
2771	8^{+11}_{-7}	$3.2^{+0.7}_{-1.0}$	27^{+20}_{-10}	38^{+63}_{-17}	20^{+4}_{-4}	65^{+20}_{-20}	24 (39)
2773	31^{+11}_{-8}	$10.7^{+2.1}_{-5.9}$	3^{+2}_{-2}	18^{+8}_{-6}	43^{+7}_{-7}	262^{+29}_{-29}	53 (57)
2800A	12^{+18}_{-10}	$4.7^{+1.1}_{-1.2}$	12^{+5}_{-8}	32^{+29}_{-7}	15^{+2}_{-2}	79^{+17}_{-17}	14 (25)
2800B	22^{+16}_{-10}	...	...	16^{+4}_{-3}	15^{+2}_{-2}	50^{+7}_{-7}	22 (29)
2802	16^{+12}_{-8}	$6.9^{+0.9}_{-0.6}$	13^{+4}_{-4}	36^{+16}_{-9}	37^{+3}_{-3}	343^{+44}_{-44}	53 (62)
2806	17^{+19}_{-10}	...	...	19^{+6}_{-5}	24^{+3}_{-4}	86^{+7}_{-12}	13 (26)
2812	16^{+22}_{-11}	$4.0^{+1.0}_{-1.7}$	21^{+27}_{-14}	30^{+17}_{-8}	29^{+5}_{-5}	147^{+29}_{-29}	25 (35)
3259	17^{+6}_{-5}	$4.8^{+0.5}_{-0.3}$	22^{+5}_{-6}	22^{+5}_{-6}	53^{+3}_{-3}	250^{+15}_{-15}	21 (43)
3291	25^{+16}_{-10}	...	...	19^{+5}_{-4}	32^{+4}_{-4}	132^{+16}_{-16}	20 (23)
3303	11^{+5}_{-4}	$5.2^{+2.9}_{-1.0}$	9^{+5}_{-7}	29^{+6}_{-4}	30^{+2}_{-2}	151^{+14}_{-14}	46 (52)
3305	23^{+15}_{-10}	...	...	21^{+4}_{-4}	16^{+2}_{-2}	72^{+8}_{-8}	26 (30)
3326	15^{+8}_{-6}	$3.5^{+0.5}_{-0.7}$	27^{+12}_{-8}	28^{+7}_{-5}	35^{+3}_{-3}	148^{+13}_{-13}	48 (61)
3329	<29	...	...	31^{+20}_{-11}	10^{+4}_{-4}	37^{+10}_{-10}	8 (11)
3331	18^{+10}_{-7}	...	...	22^{+3}_{-3}	27^{+3}_{-2}	114^{+9}_{-9}	16 (36)
3340	<26	$4.6^{+0.6}_{-0.5}$	23^{+5}_{-9}	>13	30^{+6}_{-6}	124^{+37}_{-37}	17 (30)
3343	24^{+20}_{-11}	...	...	35^{+11}_{-8}	13^{+3}_{-2}	98^{+15}_{-15}	16 (19)
3344	18^{+24}_{-15}	$9.9^{+3.5}_{-1.5}$	5^{+2}_{-3}	4^{+69}_{-2}	15^{+11}_{-11}	127^{+35}_{-35}	16 (20)
3346	<63	$9.5^{+2.8}_{-2.3}$	4^{+2}_{-2}	31^{+96}_{-30}	7^{+2}_{-2}	84^{+35}_{-35}	15 (23)
3347A	38^{+43}_{-23}	$10.4^{+1.3}_{-0.7}$	6^{+1}_{-2}	6^{+19}_{-3}	25^{+14}_{-14}	229^{+20}_{-20}	57 (61)
3348	17^{+28}_{-15}	$6.2^{+2.2}_{-1.0}$	15^{+4}_{-9}	28^{+31}_{-10}	44^{+8}_{-8}	313^{+79}_{-79}	16 (31)
3350	24^{+68}_{-21}	$9.4^{+1.4}_{-1.0}$	5^{+1}_{-2}	7^{+22}_{-4}	14^{+10}_{-10}	113^{+20}_{-20}	22 (27)
3351	16^{+11}_{-8}	$6.6^{+0.4}_{-0.3}$	21^{+3}_{-3}	35^{+15}_{-7}	62^{+5}_{-5}	579^{+39}_{-39}	49 (59)
3352	<19	$4.4^{+0.5}_{-0.5}$	25^{+6}_{-9}	>15	31^{+5}_{-5}	122^{+43}_{-43}	9 (28)
3355	34^{+21}_{-13}	...	...	15^{+4}_{-3}	40^{+5}_{-5}	152^{+25}_{-25}	35 (43)
3356	<15	$5.8^{+1.5}_{-0.8}$	18^{+7}_{-8}	37^{+85}_{-19}	47^{+18}_{-18}	237^{+129}_{-129}	14 (29)
3359	<23	$6.9^{+0.5}_{-0.5}$	26^{+4}_{-5}	>31	78^{+10}_{-10}	851^{+98}_{-77}	44 (53)
3363	<29	$4.4^{+1.6}_{-1.1}$	21^{+10}_{-18}	>11	25^{+6}_{-6}	118^{+42}_{-42}	13 (27)
3365A	64^{+18}_{-15}	...	...	19^{+3}_{-3}	44^{+6}_{-6}	360^{+27}_{-27}	16 (22)
3368B	12^{+5}_{-4}	$6.9^{+0.3}_{-0.3}$	25^{+3}_{-3}	35^{+10}_{-6}	91^{+5}_{-5}	885^{+39}_{-39}	38 (61)
3369	7^{+7}_{-5}	$4.9^{+0.5}_{-0.4}$	18^{+4}_{-5}	34^{+21}_{-9}	34^{+3}_{-3}	170^{+22}_{-22}	53 (49)
3370	31^{+49}_{-22}	$6.4^{+2.2}_{-1.0}$	7^{+4}_{-5}	5^{+14}_{-3}	11^{+8}_{-8}	40^{+13}_{-13}	16 (26)
3372	<21	$3.9^{+1.0}_{-1.7}$	22^{+11}_{-16}	36^{+62}_{-16}	27^{+5}_{-5}	113^{+46}_{-46}	27 (31)
3375	<21	$5.1^{+3.4}_{-1.1}$	11^{+6}_{-9}	28^{+27}_{-10}	20^{+3}_{-3}	92^{+18}_{-18}	30 (44)
3378	62^{+84}_{-47}	$2.0^{+1.6}_{-0.7}$	129^{+377}_{-94}	41^{+159}_{-20}	27^{+19}_{-19}	111^{+46}_{-46}	40.4 (48)
3387	14^{+9}_{-6}	$6.7^{+0.6}_{-0.5}$	24^{+5}_{-5}	28^{+9}_{-6}	98^{+6}_{-6}	794^{+56}_{-56}	43 (61)
3388	28^{+21}_{-14}	...	...	18^{+5}_{-4}	28^{+5}_{-5}	121^{+20}_{-20}	32 (33)
3399A	42^{+35}_{-22}	$5.5^{+0.9}_{-0.7}$	13^{+5}_{-4}	2^{+2}_{-1}	19^{+13}_{-13}	56^{+11}_{-11}	30 (40)
3403	21^{+38}_{-19}	$1.1^{+2.4}_{-0.2}$	193^{+812}_{-189}	29^{+18}_{-10}	11^{+4}_{-4}	36^{+8}_{-8}	17 (35)
3405	11^{+11}_{-8}	$5.8^{+2.0}_{-1.0}$	16^{+9}_{-9}	28^{+23}_{-5}	54^{+6}_{-6}	307^{+69}_{-69}	33 (32)
3412	29^{+18}_{-11}	$9.3^{+4.3}_{-1.4}$	4^{+2}_{-3}	8^{+13}_{-3}	20^{+83}_{-8}	85^{+31}_{-31}	32 (48)
3846	15^{+49}_{-14}	...	...	25^{+11}_{-8}	10^{+3}_{-3}	46^{+12}_{-12}	9 (18)
3847	15^{+25}_{-11}	...	...	23^{+9}_{-7}	7^{+1}_{-1}	31^{+6}_{-6}	4 (18)
3848	24^{+19}_{-13}	$7.2^{+1.7}_{-1.4}$	8^{+6}_{-3}	19^{+9}_{-11}	25^{+4}_{-4}	162^{+48}_{-48}	51 (51)
3851	<13	$4.9^{+0.7}_{-0.6}$	19^{+5}_{-7}	>25	25^{+7}_{-7}	130^{+67}_{-3}	16 (21)
3852	12^{+18}_{-8}	$7.6^{+1.2}_{-1.6}$	6^{+3}_{-2}	14^{+9}_{-8}	19^{+12}_{-12}	93^{+24}_{-24}	37 (47)

Table 7. (Continued.)

Trigger #*	$N_{\rm H}$† (10^{22} cm^{-2})	$kT_{\rm BB}$‡ (keV)	$R_{\rm BB}\left(\frac{d}{15\,{\rm kpc}}\right)$§ (km)	$kT_{\rm OTTB}$‖ (keV)	$F_{\rm X}$#	F_γ#	χ^2 (d.o.f.)
3854	33^{+15}_{-11}	...	...	12^{+3}_{-2}	32^{+3}_{-3}	96^{+18}_{-18}	29 (35)
3873	10^{+20}_{-5}	$4.9^{+0.5}_{-0.7}$	20^{+5}_{-7}	38^{+156}_{-16}	29^{+6}_{-6}	161^{+33}_{-33}	24 (31)
3874	16^{+11}_{-8}	$5.7^{+0.4}_{-0.3}$	24^{+4}_{-5}	28^{+13}_{-6}	57^{+3}_{-3}	411^{+32}_{-32}	28 (50)

* HETE-2 trigger number.
† Photoelectric absorption with 90% confidence level uncertainties.
‡ Blackbody temperature with 90% confidence level uncertainties.
§ Emission radius with 90% confidence level uncertainties; d is the distance to the source. We have used $d = 15$ kpc.
‖ Plasma temperature with 90% confidence level uncertainties.
X-ray (2–10 keV) and gamma-ray (10–100 keV) fluxes, 10^{-8} erg cm^{-2} s^{-1}, with 68% confidence level uncertainties.

Table 8. Spectral parameters obtained using BB+OTTB model for SGR 1900+14.

Trigger #*	$N_{\rm H}$† (10^{22} cm^{-2})	$kT_{\rm BB}$‡ (keV)	$R_{\rm BB}\left(\frac{d}{10\,{\rm kpc}}\right)$§ (km)	$kT_{\rm OTTB}$‖ (keV)	$F_{\rm X}$#	F_γ#	χ^2 (d.o.f.)
1568	41^{+30}_{-18}	...	...	$20.2^{+4.2}_{-3.4}$	27^{+5}_{-5}	164^{+18}_{-18}	24 (26)
1571	8^{+7}_{-5}	$6.4^{+0.5}_{-0.4}$	13^{+2}_{-2}	$27.3^{+6.9}_{-4.8}$	66^{+5}_{-5}	426^{+31}_{-31}	64 (58)
1572	42^{+57}_{-26}	...	...	$23.3^{+9.0}_{-5.9}$	21^{+7}_{-7}	157^{+28}_{-28}	9 (13)
1578	<37	$7.0^{+1.0}_{-0.8}$	7^{+2}_{-2}	$6.9^{+21.6}_{-6.5}$	25^{+16}_{-16}	113^{+25}_{-25}	5 (11)
2310	9^{+21}_{-8}	...	...	$17.3^{+9.9}_{-5.9}$	16^{+2}_{-2}	41^{+7}_{-7}	16 (18)

* HETE-2 trigger number.
† Photoelectric absorption with 90% confidence level uncertainties.
‡ Blackbody temperature with 90% confidence level uncertainties.
§ Emission radius with 90% confidence level uncertainties; d is the distance to the source. We have used $d = 10$ kpc.
‖ Plasma temperature with 90% confidence level uncertainties.
X-ray (2–10 keV) and gamma-ray (10–100 keV) fluxes, 10^{-8} erg cm^{-2} s^{-1}, with 68% confidence level uncertainties.

below 20 keV are somewhat different from those of the WXM. For this reason, the FREGATE spectra below 20 keV were not employed in the joint fitting. From a temporal analysis, we know that almost no emission can seen above 100 keV in most cases; We thus employed the 2–25 keV energy range for the WXM, and 20–100 keV for FREGATE.

We define the foreground time region as a burst period, and the background time region as a steady emission level (i.e., before and after the burst). The foreground time regions that included the whole burst were determined by eye. The background was selected from regions 8 seconds long at least both before and after the burst (foreground region). For two bursts, #3259 and #3303, time-resolved spectral analysis was performed, because they have sufficiently good statistics (greater than 3000 counts, 6–30 keV), and a longer durations ($\gtrsim$ 300 ms) than those of typical bursts. We used the 2BB model for these time-resolved fits. Their time histories are shown in figure 8 ($t = 0$ corresponds to the trigger time), and the best-fit spectral parameters are summarized in tables 5 and 6.

3.2.1. BB+OTTB with absorption

In some earlier studies, the hard X-ray spectra of SGR bursts were found to be well described by an OTTB function. Therefore, we tried OTTB fits, but found that they gave poor results in many cases. The discrepancies were prominent in the lower energy region for the WXM data. We thus introduced a BB component to describe the lower energies. This model gives better fits, but it requires a large absorption column to reproduce the steep turnover in the lower energy band. We find that all bursts are well reproduced by BB+OTTB, except for #3405 (15 out of 55 bursts did not require a BB component). For the remaining 40 bursts, if we fit the spectra only with OTTB, we had an excess below 5 keV. The photoelectric absorption, $N_{\rm H}$, is $\sim 10^{23}$ cm^{-2}, which is greater than the galactic value. The best-fit spectral parameters are summarized in table 7 and table 8. The quoted errors represent the 68% confidence level for fluxes and the 90% confidence level for the other parameters.

The BB temperatures, $kT_{\rm BB}$, are distributed around ~ 5 keV and the emission radii $R_{\rm BB}$ are distributed around ~ 23 km (at 15 kpc for SGR 1806−20 and at 10 kpc for SGR 1900+14). Alternatively $R'_{\rm BB} = R_{\rm BB}[d'/(15\,{\rm kpc}, 10\,{\rm kpc})]$ at an arbitrary distance of d'. The OTTB temperatures, $kT_{\rm OTTB}$ are distributed around ~ 27 keV in most cases, which is consistent with previous studies (e.g., Aptekar et al. 2001). However,

Table 9. Spectral parameters obtained using PLE model for SGR 1806−20.

Trigger #*	$N_{\rm H}$† (10^{22} cm^{-2})	α‡	E_0§ (keV)	$E_{\rm p}$‖ (keV)	$F_{\rm X}$#	F_γ#	χ^2 (d.o.f.)
1566	9^{+10}_{-6}	$0.23^{+0.42}_{-0.41}$	12^{+3}_{-2}	21^{+6}_{-4}	46^{+9}_{-9}	195^{+35}_{-35}	15.2 (35)
2770	<29	$0.44^{+0.89}_{-0.80}$	13^{+12}_{-5}	21^{+19}_{-7}	23^{+9}_{-9}	84^{+35}_{-35}	13.4 (17)
2771	23^{+21}_{-12}	$1.82^{+0.57}_{-0.70}$	>20	>10	20^{+10}_{-10}	61^{+33}_{-33}	26.2 (40)
2773	17^{+9}_{-7}	$0.48^{+0.28}_{-0.26}$	17^{+3}_{-2}	26^{+4}_{-4}	42^{+8}_{-8}	259^{+47}_{-47}	67.0 (63)
2800A	22^{+38}_{-17}	$0.86^{+0.89}_{-0.64}$	20^{+20}_{-6}	22^{+22}_{-7}	15^{+7}_{-7}	76^{+36}_{-36}	17.7 (26)
2800B	17^{+34}_{-15}	$0.74^{+1.17}_{-1.10}$	14^{+22}_{-6}	18^{+28}_{-8}	15^{+7}_{-7}	50^{+33}_{-33}	21.8 (28)
2802	13^{+13}_{-8}	$-0.02^{+0.37}_{-0.34}$	15^{+3}_{-2}	30^{+6}_{-5}	38^{+11}_{-11}	342^{+84}_{-84}	56.4 (63)
2806	<39	$0.56^{+1.11}_{-1.09}$	15^{+22}_{-6}	21^{+32}_{-9}	23^{+13}_{-13}	86^{+62}_{-62}	12.6 (25)
2812	37^{+48}_{-27}	$1.41^{+0.99}_{-0.78}$	30^{+18}_{-13}	18^{+11}_{-7}	29^{+12}_{-12}	143^{+82}_{-82}	27.4 (36)
3259	18^{+8}_{-6}	$0.38^{+0.28}_{-0.27}$	13^{+2}_{-2}	20^{+3}_{-2}	54^{+9}_{-9}	247^{+31}_{-31}	49.6 (46)
3291	29^{+41}_{-19}	$1.17^{+1.12}_{-1.07}$	21^{+76}_{-11}	18^{+62}_{-9}	32^{+21}_{-21}	133^{+86}_{-86}	19.7 (22)
3303	12^{+7}_{-5}	$0.79^{+0.24}_{-0.24}$	22^{+5}_{-4}	27^{+6}_{-4}	30^{+4}_{-4}	149^{+21}_{-21}	48.1 (53)
3305	24^{+41}_{-20}	$1.03^{+1.04}_{-0.93}$	21^{+24}_{-9}	20^{+23}_{-9}	16^{+9}_{-9}	72^{+43}_{-43}	25.5 (29)
3326	30^{+16}_{-11}	$1.47^{+0.40}_{-0.36}$	31^{+17}_{-9}	17^{+9}_{-4}	35^{+9}_{-9}	143^{+40}_{-40}	53.6 (62)
3329	<23	$1.27^{+0.71}_{-0.94}$	42^{+158}_{-27}	31^{+115}_{-19}	9^{+5}_{-5}	38^{+27}_{-27}	12.4 (15)
3331	12^{+16}_{-9}	$0.72^{+0.54}_{-0.51}$	18^{+9}_{-5}	23^{+11}_{-6}	26^{+9}_{-9}	113^{+46}_{-46}	15.4 (35)
3340	<27	$-0.63^{+1.06}_{-0.77}$	7^{+4}_{-2}	19^{+10}_{-5}	30^{+11}_{-11}	118^{+59}_{-59}	18.3 (31)
3343	22^{+31}_{-16}	$0.92^{+0.83}_{-0.78}$	32^{+85}_{-14}	35^{+92}_{-15}	13^{+7}_{-7}	98^{+69}_{-69}	16.2 (18)
3344	<24	$0.37^{+0.85}_{-0.89}$	27^{+161}_{-13}	44^{+264}_{-21}	14^{+8}_{-8}	139^{+103}_{-103}	19.6 (21)
3346	<38	$-0.21^{+0.75}_{-0.58}$	16^{+8}_{-4}	35^{+18}_{-9}	7^{+3}_{-3}	85^{+45}_{-45}	15.2 (24)
3347A	8^{+11}_{-6}	$0.18^{+0.37}_{-0.35}$	20^{+6}_{-4}	37^{+10}_{-7}	23^{+6}_{-6}	231^{+57}_{-57}	65.0 (62)
3348	<44	$0.02^{+0.73}_{-0.59}$	13^{+5}_{-3}	26^{+10}_{-5}	45^{+17}_{-17}	311^{+178}_{-178}	16.9 (32)
3350	<16	$-0.23^{+0.59}_{-0.39}$	15^{+5}_{-3}	33^{+12}_{-6}	14^{+101}_{-2}	114^{+5488}_{-46}	26.6 (28)
3351	14^{+12}_{-8}	$-0.26^{+0.31}_{-0.28}$	12^{+2}_{-1}	28^{+4}_{-3}	63^{+10}_{-10}	577^{+154}_{-154}	58.0 (60)
3352	<23	$-0.73^{+1.19}_{-0.81}$	7^{+4}_{-2}	18^{+12}_{-5}	31^{+12}_{-12}	107^{+57}_{-57}	24.5 (38)
3355	44^{+39}_{39}	$1.37^{+1.75}_{-1.42}$	19^{+154}_{-11}	12^{+97}_{-7}	40^{+24}_{-24}	154^{+133}_{-133}	34.8 (42)
3356	<15	$-0.25^{+0.61}_{-0.30}$	11^{+4}_{-2}	25^{+9}_{-4}	<94	231^{+230}_{-230}	14.4 (30)
3359	<19	$-0.78^{+0.51}_{-0.47}$	11^{+3}_{-2}	29^{+7}_{-5}	78^{+16}_{-16}	838^{+265}_{-265}	51.1 (54)
3363	30^{+59}_{-23}	$1.23^{+1.35}_{-1.06}$	22^{+123}_{-10}	16^{+95}_{-8}	27^{+18}_{-18}	110^{+72}_{-72}	15.9 (28)
3365A	67^{+26}_{-39}	$1.08^{+1.07}_{-1.04}$	19^{+22}_{-8}	18^{+21}_{-7}	44^{+30}_{-30}	360^{+282}_{-282}	16.1 (21)
3368B	7^{+5}_{-3}	$-0.55^{+0.19}_{-0.19}$	11^{+1}_{-1}	28^{+2}_{-2}	93^{+7}_{-7}	885^{+54}_{-54}	46.5 (62)
3369	8^{+8}_{-6}	$0.30^{+0.38}_{-0.37}$	14^{+4}_{-3}	24^{+6}_{-4}	35^{+5}_{-5}	163^{+20}_{-20}	53.3 (48)
3370	<40	$0.28^{+0.97}_{-0.97}$	11^{+8}_{-4}	20^{+14}_{-7}	10^{+6}_{-6}	42^{+30}_{-30}	17.8 (27)
3372	23^{+16}_{-14}	$1.38^{+0.80}_{-0.77}$	30^{+100}_{-15}	19^{+62}_{-10}	28^{+12}_{-12}	107^{+52}_{-52}	29.3 (32)
3375	10^{+19}_{-9}	$0.60^{+0.69}_{-0.67}$	17^{+12}_{-6}	24^{+17}_{-8}	20^{+6}_{-6}	89^{+42}_{-42}	32.2 (45)
3378	50^{+22}_{-14}	$1.94^{+0.06}_{-0.46}$	<57	<4	23^{+9}_{-9}	107^{+40}_{-40}	45.0 (49)
3387	8^{+8}_{-5}	$-0.33^{+0.27}_{-0.27}$	12^{+2}_{-1}	27^{+3}_{-3}	100^{+12}_{-12}	798^{+110}_{-110}	41.9 (62)
3388	<79	$0.79^{+1.69}_{-1.42}$	16^{+121}_{-8}	19^{+147}_{-9}	28^{+19}_{-19}	120^{+82}_{-82}	32.0 (32)
3399A	<23	$0.38^{+0.80}_{-0.86}$	11^{+7}_{-4}	18^{+11}_{-6}	19^{+7}_{-7}	59^{+34}_{-34}	42.4 (41)
3403	14^{+21}_{-12}	$1.65^{+0.60}_{-0.80}$	>21	>21	12^{+6}_{-6}	37^{+27}_{-27}	17.8 (36)
3405	9^{+11}_{-7}	$0.21^{+0.51}_{-0.52}$	14^{+5}_{-3}	25^{+9}_{-6}	55^{+16}_{-16}	302^{+101}_{-101}	34.5 (33)
3412	24^{+15}_{-10}	$1.19^{+0.49}_{-0.48}$	26^{+19}_{-8}	21^{+15}_{-7}	20^{+8}_{-8}	87^{+53}_{-53}	34.6 (49)
3846	<52	$0.23^{+1.21}_{-0.84}$	16^{+24}_{-6}	27^{+43}_{-11}	10^{+8}_{-8}	45^{+37}_{-37}	7.72 (17)
3847	<54	$0.62^{+1.24}_{-0.97}$	18^{+40}_{-9}	24^{+55}_{-12}	7^{+4}_{-4}	31^{+25}_{-25}	3.82 (17)
3848	12^{+14}_{-9}	$-0.12^{+0.46}_{-0.44}$	12^{+3}_{-2}	25^{+6}_{-4}	25^{+7}_{-7}	164^{+61}_{-61}	49.4 (52)
3851	<21	$-0.35^{+0.94}_{-0.53}$	10^{+6}_{-2}	23^{+15}_{-5}	25^{+9}_{-9}	116^{+74}_{-74}	19.2 (22)
3852	<13	$-0.11^{+0.48}_{-0.44}$	11^{+3}_{-2}	24^{+7}_{-5}	19^{+5}_{-5}	94^{+24}_{-24}	36.2 (48)

Table 9. (Continued.)

Trigger #*	$N_{\rm H}{}^{\dagger}$ (10^{22} cm^{-2})	$\alpha^{\ddagger}$	$E_0{}^{\S}$ (keV)	$E_{\rm p}{}^{\|}$ (keV)	$F_{\rm X}{}^{\#}$	$F_\gamma{}^{\#}$	χ^2 (d.o.f.)
3854	40^{+40}_{-23}	$1.39^{+1.30}_{-1.35}$	16^{+53}_{-8}	10^{+32}_{-5}	32^{+20}_{-20}	96^{+73}_{-73}	28.7 (34)
3873	32^{+31}_{-28}	$0.76^{+1.44}_{-1.16}$	16^{+34}_{-7}	20^{+42}_{-8}	29^{+14}_{-14}	155^{+90}_{-90}	30.0 (32)
3874	13^{+10}_{-7}	$-0.35^{+0.36}_{-0.34}$	10^{+2}_{-1}	24^{+4}_{-3}	59^{+11}_{-11}	405^{+66}_{-66}	32.4 (51)

* HETE-2 trigger number.
† Photoelectric absorption with 90% confidence level uncertainties.
‡ Spectral index with 90% confidence level uncertainties.
§ Cutoff energy with 90% confidence level uncertainties.
‖ Peak energy of the νF_ν spectrum.
X-ray (2–10 keV) and gamma-ray (10–100 keV) fluxes, 10^{-8} erg cm^{-2} s^{-1}, with 68% confidence level uncertainties.

Table 10. Spectral parameters obtained using PLE model for SGR 1900+14.

Trigger #*	$N_{\rm H}{}^{\dagger}$ (10^{22} cm^{-2})	$\alpha^{\ddagger}$	$E_0{}^{\S}$ (keV)	$E_{\rm p}{}^{\|}$ (keV)	$F_{\rm X}{}^{\#}$	$F_\gamma{}^{\#}$	χ^2 (d.o.f.)
1568	<50	$0.04^{+1.02}_{-0.93}$	13^{+5}_{-4}	25^{+10}_{-8}	26^{+17}_{-17}	159^{+110}_{-110}	21 (25)
1571	<11	$-0.26^{+0.27}_{-0.26}$	11^{+1}_{-1}	26^{+3}_{-3}	68^{+7}_{-7}	426^{+51}_{-51}	67 (59)
1572	<82	$-0.05^{+1.68}_{-1.19}$	13^{+30}_{-5}	27^{+62}_{-11}	21^{+17}_{-17}	149^{+122}_{-122}	7 (12)
1578	<17	$-0.56^{+0.67}_{-0.50}$	10^{+3}_{-2}	25^{+9}_{-5}	21^{+21}_{-21}	118^{+117}_{-117}	7 (12)
2310	<56	<2.61	>7	...	16^{+47}_{-1}	38^{+31}_{-31}	16 (17)

* HETE-2 trigger number.
† Photoelectric absorption with 90% confidence level uncertainties.
‡ Spectral index with 90% confidence level uncertainties.
§ Cutoff energy with 90% confidence level uncertainties.
‖ Peak energy of the νF_ν spectrum.
X-ray (2–10 keV) and gamma-ray (10–100 keV) fluxes, 10^{-8} erg cm^{-2} s^{-1}, with 68% confidence level uncertainties.

#3399A has a significantly smaller temperature, $kT_{\rm OTTB} \sim 2$ keV.

3.2.2. PLE with absorption

Because the OTTB model is unacceptable in many cases, we tried the PLE model; PLE can be regarded as an extension of the simple OTTB. The spectral parameters are summarized in tables 9 and 10. The quoted errors are again the 68% confidence level for the fluxes and the 90% confidence level for other parameters. We find that all bursts are well reproduced by PLE. The photoelectric absorption, $N_{\rm H}$, is $\sim 10^{23}$ cm^{-2}, again greater than the galactic value. The spectral indices, α, are distributed around ~ 0.5, which is relatively hard compared to the GRB indices. The cutoff energies, E_0, are distributed around ~ 13 keV. These spectral parameters are consistent with previous observations (Feroci et al. 2004).

3.2.3. 2BB

Some studies report that the spectra of certain SGR bursts are well reproduced by the 2BB model. In a previous study of HETE-2 samples, this model gave good fits (Nakagawa et al. 2005). In the current study, which uses all of the events available to date, 2BB again well describes the observed spectra. The spectral parameters are summarized in tables 11 and 12. The quoted errors are 68% confidence for the fluxes and 90% confidence for the other parameters, as before. Using 2BB, we obtained acceptable fits in all cases (2 out of 55 bursts did not require a higher blackbody component). Only the upper limit of the photoelectric absorption, $N_{\rm H}$, was determined for most cases (i.e., which is consistent with the galactic value). The lower blackbody temperatures, $kT_{\rm LT}$, and their radii, $R_{\rm LT}$, are distributed around ~ 4.2 keV and ~ 27 km (at 15 kpc for SGR 1806−20 and at 10 kpc for SGR 1900+14), respectively. The higher blackbody temperatures, $kT_{\rm HT}$, are generally distributed around ~ 11 keV, but for #1572, #2310, #3352, #3355, #3378, and #3851, we could only obtain lower limits. The radii of higher blackbody temperatures, $R_{\rm HT}$, are distributed around ~ 4.5 km (at 15 kpc for SGR 1806−20 and at 10 kpc for SGR 1900+14). Again $R'_{\{\rm LT,HT\}} = R_{\{\rm LT,HT\}}[d'/(15\,{\rm kpc}, 10\,{\rm kpc})]$ at an arbitrary distance of d'.

3.2.4. Disk-BB with absorption

We tried the disk-BB function because it can be regarded as an extended case of 2BB. The spectral parameters are summarized in tables 13 and 14, where the quoted errors are 68% confidence for fluxes and 90% confidence for other parameters. We find that almost all of the bursts are well reproduced by disk-BB, with some exceptions. For #3303, we find a deficit of photons around ~ 30 keV, #1571 and

Table 11. Spectral parameters obtained using 2BB model for SGR 1806−20.

Trigger #*	$N_{\rm H}$† (10^{22} cm^{-2})	$kT_{\rm LT}$‡ (keV)	$R_{\rm LT}\left(\frac{d}{15\,{\rm kpc}}\right)$§ (km)	$kT_{\rm HT}$‡ (keV)	$R_{\rm HT}\left(\frac{d}{15\,{\rm kpc}}\right)$§ (km)	$F_{\rm X}$‖	F_γ‖	χ^2 (d.o.f.)
1566	< 4	$4.3^{+0.5}_{-1.0}$	32^{+10}_{-4}	$9.7^{+3.9}_{-2.4}$	$4.5^{+5.9}_{-2.3}$	44^{+7}_{-7}	206^{+37}_{-37}	18 (34)
2770	< 6	$3.7^{+0.7}_{-0.8}$	28^{+7}_{-5}	$9.6^{+6.8}_{-2.6}$	$3.4^{+2.9}_{-2.4}$	23^{+7}_{-7}	89^{+35}_{-35}	10 (16)
2771	< 10	$3.4^{+0.5}_{-0.6}$	29^{+12}_{-7}	$13.1^{+5.6}_{-3.6}$	$1.6^{+1.5}_{-0.8}$	19^{+4}_{-4}	66^{+24}_{-24}	25 (39)
2773	5^{+5}_{-3}	$4.0^{+0.4}_{-0.4}$	36^{+6}_{-4}	$10.4^{+0.9}_{-0.8}$	$5.5^{+1.2}_{-1.1}$	43^{+1}_{-3}	271^{+20}_{-20}	38 (57)
2800A	< 9	$4.3^{+0.5}_{-0.6}$	19^{+5}_{-3}	$11.3^{+3.1}_{-2.0}$	$2.2^{+1.5}_{-1.0}$	15^{+4}_{-4}	80^{+14}_{-14}	14 (25)
2800B	< 36	$2.5^{+1.5}_{-1.2}$	36^{+123}_{-18}	$6.8^{+4.1}_{-1.7}$	$6.4^{+6.4}_{-4.7}$	15^{+8}_{-8}	48^{+20}_{-20}	23 (27)
2802	< 6	$5.4^{+0.7}_{-0.8}$	23^{+5}_{-3}	$12.0^{+3.0}_{-1.9}$	$4.2^{+2.8}_{-1.9}$	34^{+3}_{-3}	349^{+37}_{-37}	57 (62)
2806	< 48	$2.0^{+1.6}_{-0.8}$	71^{+227}_{-45}	$6.9^{+1.9}_{-1.3}$	$8.6^{+3.4}_{-4.0}$	24^{+12}_{-12}	81^{+26}_{-26}	12 (24)
2812	< 13	$4.0^{+0.5}_{-0.6}$	29^{+10}_{-6}	$11.7^{+2.5}_{-1.8}$	$2.9^{+1.5}_{-1.1}$	29^{+4}_{-4}	150^{+26}_{-26}	23 (35)
3259	3^{+3}_{-2}	$4.1^{+0.3}_{-0.4}$	38^{+5}_{-4}	$9.3^{+1.2}_{-1.0}$	$5.6^{+2.2}_{-1.7}$	52^{+2}_{-2}	255^{+19}_{-19}	26 (43)
3291	< 15	$4.0^{+0.8}_{-1.2}$	32^{+23}_{-8}	$12.4^{+19.5}_{-4.8}$	$2.3^{+2.9}_{-1.9}$	31^{+2}_{-6}	142^{+46}_{-46}	18 (21)
3303	< 3	$4.0^{+0.4}_{-0.4}$	28^{+4}_{-3}	$10.9^{+1.1}_{-0.9}$	$3.8^{+1.0}_{-0.8}$	28^{+102}_{-24}	155^{+3312}_{-76}	57 (52)
3305	< 11	$4.1^{+0.7}_{-0.9}$	20^{+9}_{-4}	$11.1^{+7.3}_{-3.1}$	$2.2^{+2.0}_{-1.4}$	16^{+5}_{-5}	75^{+31}_{-31}	25 (28)
3326	< 6	$3.7^{+0.3}_{-0.3}$	35^{+6}_{-5}	$11.7^{+1.4}_{-1.2}$	$3.0^{+0.9}_{-0.7}$	35^{+1}_{-3}	153^{+11}_{-11}	46 (61)
3329	< 12	$3.4^{+1.5}_{-1.7}$	18^{+40}_{-7}	$11.5^{+27.6}_{-4.2}$	$1.8^{+1.3}_{-1.5}$	8^{+4}_{-4}	38^{+18}_{-18}	16 (14)
3331	< 17	$2.8^{+1.0}_{-0.9}$	42^{+52}_{-15}	$8.3^{+1.6}_{-1.0}$	$6.4^{+2.1}_{-2.4}$	27^{+9}_{-9}	111^{+19}_{-19}	16 (34)
3340	< 8	$4.4^{+0.6}_{-1.6}$	26^{+9}_{-4}	10^{+27}_{-7}	$2.4^{+7.7}_{-2.2}$	30^{+4}_{-4}	124^{+58}_{-58}	16 (30)
3343	26^{+83}_{-22}	$2.1^{+1.3}_{-0.9}$	64^{+238}_{-41}	$10.4^{+1.7}_{-1.4}$	$4.1^{+1.3}_{-1.3}$	14^{+10}_{-10}	97^{+23}_{-23}	13 (17)
3344	< 42	$1.6^{+1.1}_{-0.7}$	84^{+225}_{-57}	$9.9^{+1.9}_{-1.5}$	$5.3^{+1.9}_{-1.5}$	16^{+12}_{-12}	127^{+11}_{-28}	16 (20)
3346	< 57	$3.5^{+2.2}_{-1.6}$	15^{+47}_{-7}	$10.0^{+2.4}_{-1.2}$	$4.0^{+1.8}_{-1.9}$	7^{+4}_{-4}	84^{+15}_{-15}	15 (23)
3347A	16^{+33}_{-13}	$2.3^{+0.7}_{-0.6}$	64^{+91}_{-29}	$10.3^{+0.7}_{-0.6}$	$6.5^{+0.9}_{-0.9}$	25^{+9}_{-9}	228^{+21}_{-21}	55 (61)
3348	< 14	$4.8^{+0.9}_{-1.2}$	28^{+12}_{-5}	$10.0^{+3.8}_{-1.9}$	$5.9^{+3.1}_{-3.5}$	43^{+7}_{-7}	318^{+65}_{-65}	16 (31)
3350	< 45	$2.4^{+1.1}_{-0.8}$	38^{+81}_{-19}	$9.3^{+1.0}_{-0.9}$	$5.6^{+1.3}_{-1.1}$	14^{+7}_{-7}	113^{+19}_{-19}	21 (27)
3351	< 5	$5.6^{+0.5}_{-0.5}$	30^{+4}_{-3}	$11.3^{+2.3}_{-1.4}$	$5.5^{+2.9}_{-2.3}$	61^{+2}_{-4}	587^{+58}_{-58}	49 (59)
3352	< 6	$4.5^{+0.3}_{-0.3}$	26^{+4}_{-3}	...	...	...	...	27 (39)
3355	< 27	$3.7^{+0.7}_{-0.9}$	42^{+32}_{-12}	$8.9^{+4.5}_{-2.9}$	$4.7^{+8.2}_{-3.4}$	42^{+10}_{-10}	165^{+67}_{-67}	26 (34)
3356	< 10	$4.1^{+1.1}_{-1.3}$	32^{+16}_{-9}	$8.8^{+4.9}_{-1.6}$	$7.3^{+6.2}_{-5.3}$	44^{+21}_{-21}	241^{+105}_{-105}	14 (29)
3359	< 13	$5.8^{+0.5}_{-0.5}$	30^{+6}_{-4}	$15.7^{+4.3}_{-2.7}$	$2.8^{+1.7}_{-1.2}$	66^{+10}_{-10}	634^{+77}_{-77}	40 (47)
3363	< 15	$4.5^{+0.6}_{-0.7}$	23^{+6}_{-5}	$15.8^{+20.8}_{-6.0}$	$1.1^{+2.3}_{-0.9}$	24^{+5}_{-5}	120^{+43}_{-43}	14 (27)
3365A	53^{+84}_{-42}	$2.8^{+1.9}_{-1.4}$	92^{+375}_{-58}	$7.9^{+2.8}_{-1.0}$	$12.5^{+5.3}_{-7.4}$	45^{+20}_{-20}	357^{+98}_{-98}	16 (20)
3368B	< 3	$5.7^{+0.5}_{-0.6}$	35^{+3}_{-3}	$10.8^{+2.2}_{-1.5}$	$7.6^{+4.8}_{-3.4}$	88^{+6}_{-6}	897^{+97}_{-97}	44 (61)
3369	< 2	$4.2^{+0.4}_{-0.5}$	28^{+4}_{-3}	$10.6^{+2.5}_{-1.7}$	$3.7^{+2.2}_{-1.5}$	33^{+55}_{-27}	172^{+1172}_{-123}	47 (47)
3370	20^{+45}_{-19}	$1.8^{+1.2}_{-0.7}$	61^{+153}_{-39}	$6.3^{+1.1}_{-0.9}$	$7.4^{+2.5}_{-2.5}$	11^{+6}_{-6}	40^{+9}_{-9}	15 (26)
3372	< 8	$4.0^{+0.5}_{-0.7}$	27^{+9}_{-5}	$14.1^{+6.0}_{-4.1}$	$1.7^{+1.6}_{-0.9}$	26^{+7}_{-7}	116^{+27}_{-27}	28 (31)
3375	< 7	$4.2^{+0.7}_{-1.6}$	21^{+15}_{-4}	$11.1^{+5.9}_{-3.8}$	$2.5^{+5.1}_{-1.6}$	18^{+5}_{-5}	94^{+23}_{-23}	35 (44)
3378	22^{+113}_{-19}	$3.3^{+1.0}_{-1.9}$	42^{+164}_{-18}	17^{+40}_{-10}	$1.3^{+7.0}_{-1.0}$	24^{+8}_{-8}	118^{+52}_{-52}	43 (48)
3387	< 5	$4.9^{+0.7}_{-0.8}$	41^{+8}_{-5}	$9.5^{+1.6}_{-1.1}$	$11.0^{+5.0}_{-4.4}$	97^{+3}_{-8}	811^{+98}_{-98}	41 (61)
3388	< 82	$2.2^{+1.9}_{-0.9}$	74^{+101}_{-49}	$7.0^{+2.4}_{-1.2}$	$9.8^{+5.4}_{-5.7}$	29^{+21}_{-21}	114^{+39}_{-39}	31 (31)
3399A	36^{+24}_{-22}	$1.0^{+0.5}_{-0.2}$	517^{+2725}_{-382}	$5.4^{+0.8}_{-0.6}$	$12.8^{+2.5}_{-3.7}$	19^{+1}_{-3}	56^{+9}_{-9}	30 (40)
3403	< 28	$2.0^{+1.5}_{-0.8}$	49^{+160}_{-31}	$9.6^{+4.1}_{-2.8}$	$2.7^{+1.6}_{-1.6}$	12^{+7}_{-7}	34^{+11}_{-11}	20 (35)
3405	< 11	$3.0^{+1.8}_{-1.0}$	52^{+51}_{-21}	$7.8^{+4.6}_{-1.0}$	$12.0^{+2.7}_{-8.6}$	56^{+15}_{-15}	296^{+51}_{-51}	37 (32)
3412	16^{+17}_{-10}	$2.3^{+0.7}_{-0.5}$	58^{+52}_{-24}	$8.5^{+1.1}_{-1.0}$	$5.4^{+1.6}_{-1.4}$	20^{+7}_{-7}	84^{+14}_{-14}	35 (48)
3846	< 54	$2.8^{+2.3}_{-1.7}$	23^{+100}_{-13}	$8.6^{+5.3}_{-2.0}$	$3.9^{+1.9}_{-2.7}$	10^{+8}_{-8}	44^{+37}_{-41}	8 (16)
3847	< 19	$3.6^{+1.1}_{-1.2}$	15^{+12}_{-5}	$10.1^{+7.7}_{-3.0}$	$2.0^{+2.6}_{-1.5}$	7^{+5}_{-5}	32^{+18}_{-18}	3 (16)
3848	< 9	$4.0^{+0.9}_{-1.2}$	24^{+12}_{-5}	$8.5^{+1.6}_{-1.1}$	$6.8^{+3.3}_{-2.9}$	24^{+3}_{-3}	166^{+35}_{-35}	49 (51)
3851	< 156	$4.8^{+1.0}_{-1.8}$	11^{+31}_{-4}	...	...	6^{+3}_{-3}	25^{+3}_{-9}	9 (11)
3852	< 10	$3.1^{+0.7}_{-0.9}$	28^{+20}_{-7}	$7.8^{+1.0}_{-0.9}$	$6.8^{+2.4}_{-2.0}$	20^{+7}_{-7}	94^{+17}_{-17}	34 (47)

Table 11. (Continued.)

Trigger #*	$N_{\rm H}$† (10^{22} cm^{-2})	$kT_{\rm LT}$‡ (keV)	$R_{\rm LT}\left(\frac{d}{15\,{\rm kpc}}\right)$§ (km)	$kT_{\rm HT}$‡ (keV)	$R_{\rm HT}\left(\frac{d}{15\,{\rm kpc}}\right)$§ (km)	$F_{\rm X}$‖	F_γ‖	χ^2 (d.o.f.)
3854	30^{+47}_{-26}	$1.7^{+2.2}_{-0.7}$	136^{+379}_{-102}	$5.0^{+7.4}_{-0.9}$	$18.1^{+14.8}_{-16.7}$	33^{+15}_{-15}	89^{+28}_{-28}	31 (33)
3873	< 9	$4.8^{+0.4}_{-0.6}$	24^{+6}_{-3}	$13.3^{+7.5}_{-3.8}$	$1.9^{+2.5}_{-1.1}$	29^{+136}_{-11}	162^{+16314}_{-113}	24 (31)
3874	< 4	$5.1^{+0.4}_{-0.6}$	32^{+4}_{-3}	$10.2^{+2.9}_{-1.9}$	$5.3^{+5.0}_{-2.8}$	57^{+2}_{-3}	414^{+56}_{-56}	26 (50)

* HETE-2 trigger number.
† Photoelectric absorption with 90% confidence level uncertainties.
‡ Blackbody temperatures with 90% confidence level uncertainties.
§ Emission radii with 90% confidence level uncertainties; d is the distance to the source. We have used $d = 15$ kpc.
‖ X-ray (2–10 keV) and gamma-ray (10–100 keV) fluxes, 10^{-8} erg cm^{-2} s^{-1}, with 68% confidence level uncertainties.

Table 12. Spectral parameters obtained using 2BB model for SGR 1900+14.

Trigger #*	$N_{\rm H}$† (10^{22} cm^{-2})	$kT_{\rm LT}$‡ (keV)	$R_{\rm LT}\left(\frac{d}{10\,{\rm kpc}}\right)$§ (km)	$kT_{\rm HT}$‡ (keV)	$R_{\rm HT}\left(\frac{d}{10\,{\rm kpc}}\right)$§ (km)	$F_{\rm X}$‖	F_γ‖	χ^2 (d.o.f.)
1568	< 169	$1.8^{+2.6}_{-0.6}$	76^{+245}_{-62}	$7.2^{+1.5}_{-0.8}$	$7.3^{+2.1}_{-3.2}$	28^{+21}_{-21}	149^{+23}_{-23}	20 (24)
1571	< 2	$4.8^{+0.5}_{-0.6}$	22^{+3}_{-2}	$9.7^{+1.5}_{-1.2}$	$4.8^{+2.4}_{-1.8}$	62^{+9}_{-9}	438^{+47}_{-47}	67 (58)
1572	< 93	$1.4^{+5.3}_{-0.5}$	176^{+1737}_{-164}	> 6.2	$7.1^{+1.8}_{-4.6}$	23^{+20}_{-20}	135^{+30}_{-30}	7 (11)
1578	< 30	$1.9^{+1.9}_{-1.3}$	36^{+341}_{-25}	$6.9^{+0.8}_{-0.8}$	$6.9^{+2.2}_{-1.7}$	...	...	5 (11)
2310	< 11	$3.7^{+0.5}_{-0.6}$	15^{+5}_{-4}	> 12.5	$0.3^{+0.7}_{-0.2}$	16^{+6}_{-6}	57^{+26}_{-26}	8 (16)

* HETE-2 trigger number.
† Photoelectric absorption with 90% confidence level uncertainties.
‡ Blackbody temperatures with 90% confidence level uncertainties.
§ Emission radii with 90% confidence level uncertainties; d is the distance to the source. We have used $d = 10$ kpc.
‖ X-ray (2–10 keV) and gamma-ray (10–100 keV) fluxes, 10^{-8} erg cm^{-2} s^{-1}, with 68% confidence level uncertainties.

#3368B show an excess below ~ 5 keV, while #3326 shows an excess above ~ 50 keV. The photoelectric absorption, $N_{\rm H}$, is $\sim 10^{23}$ cm^{-2}, which is greater than the galactic value. The temperatures at the inner disk radius, $T_{\rm in}$, are distributed around ~ 10 keV, and the values of $R_{\rm in}\sqrt{\cos\theta}$ are distributed around ~ 4.5 km (at 15 kpc for SGR 1806−20 and at 10 kpc for SGR 1900+14), where $R_{\rm in}$ denotes the inner disk radius and θ denotes the angle of the disk. As before, $R'_{\rm in}\sqrt{\cos\theta} = R_{\rm in}\sqrt{\cos\theta}[d'/(15\,{\rm kpc}, 10\,{\rm kpc})]$ at an arbitrary distance d'.

3.2.5. BB+PL with absorption

The 2BB or disk-BB fits suggest that reprocessed X-ray emission may be present in the spectra. Another possibility is inverse Compton scattering by a medium, such as a hot plasma. The spectral parameters are summarized in tables 15 and 16. The quoted errors are 68% confidence for the fluxes and 90% confidence for the other parameters. We find that all of the bursts are well reproduced by BB+PL, except for #3326, which has an excess below 5 keV. The photoelectric absorption, $N_{\rm H}$ is on the order of $\sim 10^{23}$ cm^{-2}, which is greater than the galactic value. The blackbody temperatures, $kT_{\rm BB}$, are distributed around ~ 5.5 keV and the blackbody radii, $R_{\rm BB}$, are distributed around ~ 13 km (at 15 kpc for SGR 1806−20 and at 10 kpc for SGR 1900+14). $R'_{\rm BB} = R_{\rm BB}[d'/(15\,{\rm kpc}, 10\,{\rm kpc})]$ at an arbitrary distance of d'. The spectral indices, α, for the PL component are distributed around ~ 2.1.

4. Discussion

4.1. Cumulative Number–Intensity Distribution for SGR 1806−20

The cumulative number–intensity distribution for 2–100 keV fluences was calculated for the short bursts from SGR 1806−20. The fluences were derived from the 2BB fits. Poor statistics of the single peaked bursts did not allow us to investigate their distributions separately from those of the multiple peaked bursts. Therefore, we investigated the distribution using both burst samples.

In figure 9 (p.673), the dashed stepwise line represents the observational data, and the solid stepwise line represents the data corrected for observational efficiencies, which are derived in section 2. These cumulative number–intensity distributions were shown to be flattened below 4×10^{-7} erg cm^{-2}. For the WXM instrument, the threshold sensitivity for localization is of 3×10^{-7} erg cm^{-2} in the 2–25 keV (Shirasaki et al. 2003), which corresponds to $\sim 4 \times 10^{-7}$ erg cm^{-2} in the 2–100 keV band, and hence the apparent flattening is thought to be due to an instrumental selection effect.

The cumulative distribution is well described by a single

Table 13. Spectral parameters obtained using disk-BB model for SGR 1806−20.

Trigger #*	$N_{\rm H}$†	$T_{\rm in}$‡	$R_{\rm in}\sqrt{\cos\theta}\left(\frac{d}{15\,{\rm kpc}}\right)$§	$F_{\rm X}$‖	F_γ‖	χ^2 (d.o.f.)
	(10^{22} cm^{-2})	(keV)	(km)			
1566	10^{+5}_{-4}	$9.4^{+0.6}_{-0.6}$	$6.1^{+1.0}_{-0.8}$	46^{+4}_{-4}	193^{+11}_{-11}	17 (36)
2770	7^{+8}_{-5}	$9.1^{+1.2}_{-1.1}$	$4.3^{+1.4}_{-1.0}$	23^{+3}_{-3}	83^{+12}_{-12}	15 (18)
2771	8^{+8}_{-5}	$7.6^{+1.5}_{-1.2}$	$5.2^{+2.3}_{-1.7}$	19^{+3}_{-3}	53^{+10}_{-10}	37 (41)
2773	14^{+4}_{-3}	$11.5^{+0.6}_{-0.6}$	$4.5^{+0.6}_{-0.5}$	42^{+2}_{-2}	259^{+10}_{-10}	58 (59)
2800A	9^{+8}_{-5}	$10.7^{+1.1}_{-1.0}$	$2.8^{+0.7}_{-0.5}$	15^{+2}_{-2}	73^{+6}_{-6}	23 (27)
2800B	10^{+12}_{-7}	$8.2^{+1.4}_{-1.2}$	$4.2^{+1.7}_{-1.2}$	14^{+3}_{-3}	49^{+11}_{-11}	23 (29)
2802	23^{+9}_{-7}	$12.9^{+0.8}_{-0.8}$	$4.1^{+0.6}_{-0.5}$	38^{+3}_{-3}	342^{+16}_{-16}	59 (64)
2806	7^{+13}_{-7}	$9.4^{+1.9}_{-1.6}$	$4.0^{+2.0}_{-1.3}$	22^{+5}_{-5}	85^{+25}_{-25}	13 (26)
2812	7^{+8}_{-5}	$11.3^{+1.3}_{-1.2}$	$3.4^{+0.9}_{-0.7}$	26^{+4}_{-4}	133^{+12}_{-12}	37 (37)
3259	15^{+3}_{-3}	$9.2^{+0.4}_{-0.4}$	$7.2^{+0.7}_{-0.6}$	53^{+2}_{-2}	240^{+7}_{-7}	39 (45)
3291	15^{+13}_{-8}	$8.6^{+1.6}_{-1.4}$	$5.9^{+2.7}_{-1.8}$	31^{+6}_{-6}	126^{+29}_{-29}	23 (23)
3303	6^{+3}_{-2}	$12.1^{+0.7}_{-0.6}$	$3.0^{+0.4}_{-0.3}$	27^{+2}_{-2}	146^{+6}_{-6}	66 (54)
3305	10^{+10}_{-6}	$9.8^{+1.5}_{-1.3}$	$3.3^{+1.2}_{-0.9}$	16^{+2}_{-2}	69^{+11}_{-11}	29 (30)
3326	7^{+4}_{-3}	$10.1^{+0.9}_{-0.8}$	$4.3^{+0.9}_{-0.7}$	31^{+2}_{-2}	134^{+8}_{-8}	92 (63)
3329	<9	$12.0^{+2.8}_{-2.5}$	$1.5^{+0.9}_{-0.5}$	8^{+3}_{-3}	36^{+9}_{-9}	16 (16)
3331	6^{+6}_{-4}	$10.7^{+1.1}_{-1.0}$	$3.4^{+0.8}_{-0.7}$	25^{+3}_{-3}	111^{+10}_{-10}	18 (36)
3340	20^{+13}_{-9}	$7.7^{+0.9}_{-0.8}$	$7.5^{+2.3}_{-1.7}$	30^{+3}_{-3}	117^{+14}_{-14}	20 (32)
3343	13^{+15}_{-8}	$15.4^{+2.8}_{-2.5}$	$1.5^{+0.6}_{-0.4}$	11^{+3}_{-3}	99^{+20}_{-20}	17 (19)
3344	6^{+14}_{-6}	$18.6^{+5.9}_{-3.8}$	$1.2^{+0.6}_{-0.5}$	14^{+6}_{-6}	137^{+61}_{-61}	19 (22)
3346	24^{+24}_{-14}	$15.2^{+2.1}_{-1.9}$	$1.4^{+0.5}_{-0.3}$	7^{+2}_{-2}	84^{+11}_{-111}	16 (25)
3347A	13^{+7}_{-5}	$16.1^{+1.3}_{-1.2}$	$2.1^{+0.3}_{-0.3}$	24^{+3}_{-3}	230^{+18}_{-18}	63 (63)
3348	22^{+14}_{-9}	$11.0^{+0.9}_{-0.9}$	$5.5^{+1.2}_{-0.9}$	45^{+7}_{-7}	310^{+24}_{-24}	18 (33)
3350	13^{+13}_{-8}	$14.0^{+1.7}_{-1.6}$	$1.9^{+0.5}_{-0.4}$	14^{+3}_{-3}	112^{+17}_{-17}	27 (29)
3351	34^{+7}_{-6}	$11.5^{+0.5}_{-0.4}$	$6.9^{+0.7}_{-0.6}$	62^{+5}_{-4}	581^{+16}_{-16}	66 (61)
3352	16^{+16}_{-9}	$7.5^{+1.1}_{-1.0}$	$7.5^{+3.2}_{-2.0}$	31^{+5}_{-5}	106^{+18}_{-18}	27 (39)
3355	22^{+17}_{-10}	$7.4^{+1.4}_{-1.2}$	$9.2^{+4.8}_{-3.0}$	39^{+8}_{-8}	146^{+29}_{-29}	38 (43)
3356	<26	$10.7^{+1.2}_{-1.2}$	$5.0^{+1.6}_{-1.1}$	48^{+8}_{-8}	230^{+28}_{-28}	17 (31)
3359	43^{+20}_{-16}	$11.9^{+1.0}_{-1.0}$	$7.7^{+1.7}_{-1.3}$	74^{+10}_{-10}	852^{+60}_{-60}	59 (55)
3363	12^{+14}_{-8}	$9.0^{+1.5}_{-1.2}$	$4.9^{+2.0}_{-1.4}$	25^{+5}_{-5}	104^{+18}_{-18}	19 (29)
3365A	38^{+15}_{-12}	$10.0^{+1.2}_{-1.1}$	$7.2^{+2.1}_{-1.6}$	43^{+8}_{-8}	349^{+42}_{-42}	19 (22)
3368B	34^{+6}_{-5}	$11.6^{+0.4}_{-0.4}$	$8.3^{+0.7}_{-0.6}$	93^{+4}_{-4}	887^{+20}_{-20}	79 (63)
3369	9^{+4}_{-3}	$10.3^{+0.7}_{-0.7}$	$4.5^{+0.7}_{-0.6}$	34^{+2}_{-2}	161^{+10}_{-10}	57 (49)
3370	14^{+13}_{-8}	$8.6^{+1.3}_{-1.2}$	$3.4^{+1.3}_{-0.9}$	10^{+2}_{-2}	42^{+8}_{-8}	17 (28)
3372	8^{+8}_{-5}	$9.2^{+1.6}_{-1.3}$	$4.5^{+1.7}_{-1.3}$	26^{+5}_{-5}	100^{+15}_{-15}	36 (33)
3375	7^{+7}_{-4}	$10.4^{+1.3}_{-1.2}$	$3.3^{+0.9}_{-0.7}$	20^{+2}_{-2}	87^{+9}_{-9}	34 (46)
3378	25^{+22}_{-15}	$7.6^{+2.9}_{-1.9}$	$6.8^{+6.6}_{-3.5}$	21^{+7}_{-7}	88^{+30}_{-30}	55 (50)
3387	26^{+8}_{-6}	$11.3^{+0.5}_{-0.5}$	$8.2^{+0.9}_{-0.8}$	101^{+6}_{-6}	799^{+31}_{-31}	52 (63)
3388	13^{+16}_{-9}	$9.1^{+1.6}_{-1.4}$	$5.1^{+2.4}_{-1.6}$	27^{+6}_{-6}	118^{+27}_{-27}	33 (33)
3399A	9^{+8}_{-5}	$8.2^{+1.0}_{-0.9}$	$4.6^{+1.4}_{-1.0}$	18^{+3}_{-3}	59^{+12}_{-12}	41 (42)
3403	<9	$10.7^{+3.2}_{-2.7}$	$1.9^{+1.5}_{-0.8}$	10^{+3}_{-3}	35^{+14}_{-14}	25 (37)
3405	12^{+7}_{-5}	$10.9^{+1.1}_{-1.0}$	$5.5^{+1.2}_{-1.0}$	55^{+6}_{-6}	299^{+30}_{-30}	35 (34)
3412	11^{+6}_{-4}	$10.4^{+1.2}_{-1.1}$	$3.2^{+0.8}_{-0.6}$	17^{+2}_{-2}	85^{+10}_{-10}	45 (50)
3846	<25	$12.1^{+3.0}_{-2.5}$	$1.7^{+1.1}_{-0.6}$	10^{+4}_{-4}	45^{+13}_{-13}	68 (18)
3847	<19	$10.7^{+2.6}_{-2.2}$	$1.8^{+1.1}_{-0.7}$	7^{+2}_{-2}	30^{+6}_{-6}	5 (18)
3848	22^{+8}_{-6}	$10.6^{+0.8}_{-0.7}$	$4.3^{+0.7}_{-0.6}$	25^{+2}_{-2}	164^{+12}_{-12}	50 (53)
3851	11^{+15}_{-8}	$9.9^{+1.6}_{-1.5}$	$4.2^{+1.8}_{-1.2}$	25^{+4}_{-4}	116^{+20}_{-20}	21 (23)
3852	9^{+8}_{-5}	$10.4^{+1.0}_{-1.0}$	$3.4^{+0.8}_{-0.6}$	20^{+3}_{-3}	94^{+10}_{-10}	37 (49)

Table 13. (Continued.)

Trigger #*	$N_{\rm H}$†	$T_{\rm in}$‡	$R_{\rm in}\sqrt{\cos\theta}\left(\frac{d}{15\,{\rm kpc}}\right)$§	$F_{\rm X}$‖	F_γ‖	χ^2 (d.o.f.)
	($10^{22}\,{\rm cm}^{-2}$)	(keV)	(km)			
3854	22^{+12}_{-8}	$6.5^{+0.9}_{-0.8}$	$10.0^{+3.8}_{-2.7}$	31^{+7}_{-7}	94^{+20}_{-20}	31 (35)
3873	19^{+12}_{-8}	$9.5^{+1.1}_{-1.0}$	$5.3^{+1.6}_{-1.1}$	29^{+3}_{-3}	151^{+21}_{-21}	32 (33)
3874	30^{+6}_{-5}	$9.8^{+0.4}_{-0.4}$	$8.1^{+0.9}_{-0.8}$	59^{+3}_{-3}	406^{+13}_{-13}	39 (52)

* HETE-2 trigger number.
† Photoelectric absorption with 90% confidence level uncertainties.
‡ Inner disk radius temperature with 90% confidence level uncertainties.
§ $R_{\rm in}$ is the inner disk radius, θ is the angle of the disk, and d is the distance to the source.
We used $d = 15\,{\rm kpc}$. The quoted uncertainties are for 90% confidence.
‖ X-ray (2–10 keV) and gamma-ray (10–100 keV) fluxes, $10^{-8}\,{\rm erg\,cm^{-2}\,s^{-1}}$, with 68% confidence level uncertainties.

Table 14. Spectral parameters obtained using disk-BB model for SGR 1900+14.

Trigger #*	$N_{\rm H}$†	$T_{\rm in}$‡	$R_{\rm in}\sqrt{\cos\theta}\left(\frac{d}{10\,{\rm kpc}}\right)$§	$F_{\rm X}$‖	F_γ‖	χ^2 (d.o.f.)
	($10^{22}\,{\rm cm}^{-2}$)	(keV)	(km)			
1568	18^{+21}_{-11}	$10.5^{+1.4}_{-1.2}$	$2.9^{+0.9}_{-0.7}$	26^{+7}_{-7}	158^{+24}_{-24}	21 (26)
1571	17^{+7}_{-5}	$10.8^{+0.5}_{-0.5}$	$4.4^{+0.5}_{-0.4}$	69^{+4}_{-4}	427^{+15}_{-15}	75 (60)
1572	20^{+41}_{-17}	$11.4^{+2.4}_{-1.9}$	$2.4^{+1.2}_{-0.8}$	21^{+8}_{-8}	149^{+42}_{-42}	7 (13)
1578	<46	$10.2^{+1.4}_{-1.3}$	$2.6^{+1.1}_{-0.7}$	23^{+6}_{-6}	117^{+22}_{-22}	10 (13)
2310	<23	$7.1^{+2.1}_{-1.5}$	$3.4^{+2.5}_{-1.5}$	16^{+5}_{-5}	38^{+13}_{-13}	16 (18)

* HETE-2 trigger number.
† Photoelectric absorption with 90% confidence level uncertainties.
‡ Inner disk radius temperature with 90% confidence level uncertainties.
§ $R_{\rm in}$ is the inner disk radius, θ is the angle of the disk, and d is the distance to the source. We used $d = 10\,{\rm kpc}$. The quoted uncertainties are for 90% confidence.
‖ X-ray (2–10 keV) and gamma-ray (10–100 keV) fluxes, $10^{-8}\,{\rm erg\,cm^{-2}\,s^{-1}}$, with 68% confidence level uncertainties.

power-law model with a slope of -1.4 ± 0.4 after a correction for the efficiency using the data above $4 \times 10^{-7}\,{\rm erg\,cm^{-2}}$. Here, the quoted error is for 90% confidence. The fitting result is represented by the solid straight line in figure 9. This slope is steeper than those obtained previously. KONUS results gave a slope of -0.9 using 26 bursts with fluences above $\sim 10^{-6}\,{\rm erg\,cm^{-2}}$, which were observed between 1979 January and 1999 June (Aptekar et al. 2001). The INTEGRAL result was -0.91 ± 0.09 in the 15–100 keV range using 224 bursts with fluences above $3 \times 10^{-8}\,{\rm erg\,cm^{-2}}$ during the period between 2003 March and 2004 October (Götz et al. 2006). BATSE results gave a somewhat flatter distribution with -0.76 ± 0.17 based on 92 bursts with fluences between 5.0×10^{-8} and $4.3 \times 10^{-6}\,{\rm erg\,cm^{-2}}$ observed between 1993 September and 1999 June (Göğüş et al. 2000). ICE results gave -0.67 ± 0.15 using 113 bursts with fluences between 1.8×10^{-7} and $6.5 \times 10^{-6}\,{\rm erg\,cm^{-2}}$ recorded between 1979 January and 1984 June (Göğüş et al. 2000). The RXTE result was the flattest with an index of -0.43 ± 0.06 for 266 bursts with fluences between 1.7×10^{-10} and $1.9 \times 10^{-7}\,{\rm erg\,cm^{-2}}$, detected between 1996 November 5 and 1996 November 18 (Göğüş et al. 2000).

One possible explanation for these differences could be the different energy bands of the various experiments. To investigate the energy dependence of the slope, we calculated the cumulative distributions in two different bands, 2–10 keV and 10–100 keV. One can see a flattening below $6 \times 10^{-8}\,{\rm erg\,cm^{-2}}$ for 2–10 keV and $3 \times 10^{-7}\,{\rm erg\,cm^{-2}}$ for 10–100 keV. The threshold sensitivity for localization corresponds to $5.0 \times 10^{-8}\,{\rm erg\,cm^{-2}}$ for 2–10 keV and $3.0 \times 10^{-7}\,{\rm erg\,cm^{-2}}$ for 10–100 keV (Shirasaki et al. 2003). We thus restricted the fits to fluences above $6 \times 10^{-8}\,{\rm erg\,cm^{-2}}$ for 2–10 keV and $3 \times 10^{-7}\,{\rm erg\,cm^{-2}}$ for 10–100 keV. In both energy bands, the distributions are well described by a single power-law model. The best-fit slopes are -1.6 ± 0.5 for 2–10 keV and -1.4 ± 0.4 for 10–100 keV, where the quoted errors again correspond to 90% confidence. Thus, while there could be a slight energy dependence, it is not significant and does not fully explain these differences.

Another possibility is the intrinsic activity of SGRs, which would have been sampled differently by previous experiments, since they took data over different periods. Although the observing period of HETE-2 overlapped with that of INTEGRAL, the HETE-2 bursts were distributed in June and

Table 15. Spectral parameters obtained using BB+PL model for SGR 1806−20.

Trigger #*	$N_{\rm H}$†	$kT_{\rm BB}$‡	$R_{\rm BB}\left(\frac{d}{15\,{\rm kpc}}\right)$§	α‖	$F_{\rm X}$#	F_γ#	χ^2 (d.o.f.)
	($10^{22}\,{\rm cm}^{-2}$)	(keV)	(km)				
1566	$16^{+12}_{-1.0}$	$5.4^{+0.5}_{-0.4}$	19^{+4}_{-4}	$2.1^{+0.3}_{-0.3}$	45^{+7}_{-7}	202^{+23}_{-23}	10 (34)
2770	<24	$4.5^{+0.7}_{-0.5}$	18^{+5}_{-6}	$1.6^{+0.5}_{-0.6}$	23^{+7}_{-7}	93^{+35}_{-35}	11 (16)
2771	18^{+19}_{-12}	$3.8^{+1.8}_{-1.0}$	18^{+13}_{-13}	$2.1^{+0.4}_{-0.5}$	20^{+7}_{-7}	63^{+24}_{-24}	24 (39)
2773	56^{+56}_{-26}	$7.6^{+1.7}_{-1.2}$	10^{+5}_{-2}	$2.7^{+0.6}_{-0.4}$	42^{+9}_{-9}	254^{+38}_{-38}	84 (57)
2800A	21^{+46}_{-18}	$5.3^{+1.3}_{-0.7}$	11^{+4}_{-5}	$2.0^{+0.6}_{-0.5}$	15^{+4}_{-4}	79^{+23}_{-23}	18 (25)
2800B	34^{+57}_{-26}	$5.3^{+2.3}_{-1.2}$	9^{+7}_{-6}	$2.6^{+1.3}_{-0.7}$	14^{+5}_{-5}	50^{+18}_{-18}	22 (27)
2802	24^{+19}_{-11}	$7.3^{+0.6}_{-0.5}$	14^{+2}_{-2}	$2.0^{+0.3}_{-0.3}$	37^{+7}_{-7}	338^{+45}_{-45}	55 (62)
2806	27^{+32}_{-22}	$6.3^{+2.0}_{-1.7}$	9^{+8}_{-5}	$2.6^{+1.1}_{-0.8}$	23^{+10}_{-10}	86^{+34}_{-34}	13 (24)
2812	89^{+60}_{-76}	<16.3	<9	$2.8^{+0.9}_{-1.0}$	27^{+12}_{-12}	148^{+57}_{-57}	30 (35)
3259	30^{+11}_{-9}	$5.5^{+0.3}_{-0.3}$	21^{+3}_{-3}	$2.4^{+0.2}_{-0.2}$	52^{+4}_{-4}	245^{+13}_{-13}	41 (43)
3291	23^{+33}_{-22}	$4.4^{+1.5}_{-0.8}$	22^{+12}_{-12}	$2.0^{+0.6}_{-1.2}$	31^{+12}_{-12}	140^{+56}_{-56}	18 (21)
3303	20^{+9}_{-7}	$6.8^{+0.9}_{-0.8}$	9^{+3}_{-2}	$2.1^{+0.2}_{-0.2}$	30^{+3}_{-3}	147^{+12}_{-12}	54 (52)
3305	26^{+38}_{-25}	$5.1^{+1.9}_{-0.5}$	11^{+6}_{-7}	$2.1^{+0.6}_{-0.7}$	16^{+6}_{-6}	74^{+27}_{-27}	24 (28)
3326	40^{+52}_{-16}	$5.2^{+5.7}_{-1.0}$	12^{+9}_{-10}	$2.4^{+0.7}_{-0.3}$	35^{+8}_{-8}	142^{+26}_{-26}	65 (61)
3329	<33	$5.3^{+5.2}_{-1.3}$	<19	$1.8^{+0.6}_{-0.7}$	9^{+3}_{-3}	39^{+13}_{-13}	11 (14)
3331	32^{+31}_{-16}	$7.2^{+1.3}_{-1.3}$	7^{+3}_{-2}	$2.5^{+0.7}_{-0.4}$	26^{+7}_{-7}	110^{+24}_{-24}	17 (34)
3340	<39	$4.7^{+0.4}_{-0.4}$	24^{+4}_{-5}	$1.8^{+1.0}_{-4.8}$	29^{+12}_{-12}	125^{+32}_{-32}	18 (30)
3343	56^{+97}_{-33}	$10.7^{+2.0}_{-1.0}$	4^{+2}_{-1}	$3.2^{+1.1}_{-1.2}$	14^{+12}_{-12}	97^{+23}_{-23}	12 (17)
3344	22^{+32}_{-18}	$10.1^{+2.5}_{-1.7}$	5^{+2}_{-2}	$2.9^{+2.8}_{-1.6}$	15^{+12}_{-12}	129^{+28}_{-28}	16 (20)
3346	24^{+122}_{-23}	$8.9^{+1.9}_{-1.6}$	5^{+2}_{-2}	$1.9^{+2.3}_{-0.7}$	7^{+4}_{-4}	84^{+24}_{-24}	16 (23)
3347A	48^{+50}_{-24}	$10.4^{+0.8}_{-1.0}$	6^{+1}_{-1}	$2.7^{+0.9}_{-0.6}$	24^{+12}_{-12}	229^{+29}_{-29}	58 (61)
3348	28^{+52}_{-24}	$6.6^{+0.9}_{-0.7}$	16^{+5}_{-5}	$2.2^{+0.7}_{-0.7}$	43^{+16}_{-16}	309^{+56}_{-56}	18 (31)
3350	40^{+74}_{-29}	$9.2^{+1.0}_{-1.0}$	5^{+1}_{-1}	$2.8^{+1.5}_{-0.8}$	13^{+10}_{-10}	113^{+16}_{-16}	24 (27)
3351	23^{+16}_{-11}	$6.8^{+0.3}_{-0.3}$	22^{+2}_{-2}	$2.0^{+0.3}_{-0.3}$	61^{+11}_{-11}	573^{+59}_{-59}	53 (59)
3352	<28	$4.4^{+0.5}_{-0.4}$	26^{+6}_{-6}	$1.7^{+0.9}_{-2.4}$	31^{+12}_{-12}	116^{+44}_{-44}	21 (37)
3355	32^{+86}_{-25}	$4.0^{+5.8}_{-1.5}$	<37	$2.2^{+1.2}_{-1.4}$	39^{+19}_{-19}	164^{+81}_{-81}	34 (41)
3356	<19	$5.9^{+1.0}_{-0.7}$	18^{+6}_{-5}	$1.6^{+0.6}_{-0.4}$	46^{+20}_{-20}	238^{+87}_{-87}	14 (29)
3359	<37	$7.1^{+0.5}_{-0.5}$	25^{+4}_{-4}	$1.8^{+0.5}_{-1.0}$	79^{+21}_{-21}	844^{+121}_{-121}	43 (53)
3363	27^{+42}_{-22}	$5.0^{+1.4}_{-0.9}$	15^{+9}_{-7}	$2.2^{+0.5}_{-0.7}$	26^{+11}_{-11}	115^{+42}_{-42}	11 (27)
3365A	136^{+42}_{-59}	$7.7^{+1.4}_{-1.7}$	10^{+6}_{-5}	$3.3^{+1.0}_{-0.7}$	43^{+10}_{-10}	362^{+68}_{-68}	16 (20)
3368B	16^{+7}_{-6}	$7.0^{+0.2}_{-0.2}$	26^{+2}_{-2}	$1.9^{+0.2}_{-0.2}$	90^{+9}_{-9}	879^{+53}_{-53}	43 (61)
3369	10^{+11}_{-7}	$5.3^{+0.5}_{-0.4}$	18^{+3}_{-4}	$1.8^{+0.3}_{-0.3}$	33^{+5}_{-5}	171^{+23}_{-23}	50 (47)
3370	44^{+53}_{-26}	$6.1^{+1.1}_{-1.0}$	7^{+4}_{-3}	$3.2^{+1.6}_{-0.9}$	10^{+7}_{-7}	41^{+12}_{-12}	17 (26)
3372	19^{+13}_{-14}	$4.7^{+1.6}_{-0.9}$	16^{+9}_{-9}	$2.0^{+0.4}_{-0.5}$	27^{+8}_{-8}	111^{+38}_{-38}	27 (31)
3375	19^{+22}_{-13}	$5.8^{+1.3}_{-0.9}$	10^{+5}_{-4}	$2.1^{+0.5}_{-0.4}$	20^{+4}_{-4}	91^{+17}_{-17}	29 (44)
3378	80^{+89}_{-56}	$1.8^{+1.6}_{-0.3}$	174^{+487}_{-152}	$2.1^{+0.6}_{-0.9}$	26^{+17}_{-17}	113^{+58}_{-58}	40 (48)
3387	19^{+11}_{-8}	$6.9^{+0.4}_{-0.4}$	26^{+3}_{-3}	$2.1^{+0.3}_{-0.3}$	95^{+17}_{-17}	785^{+54}_{-54}	50 (61)
3388	<109	$5.9^{+2.3}_{-1.6}$	11^{+13}_{-7}	$2.6^{+1.4}_{-1.7}$	28^{+14}_{-14}	123^{+47}_{-47}	31 (31)
3399A	54^{+24}_{-26}	$5.6^{+1.1}_{-0.7}$	12^{+4}_{-3}	$5.1^{+0.7}_{-1.9}$	19^{+2}_{-2}	56^{+10}_{-10}	30 (40)
3403	23^{+32}_{-15}	<22.8	<7	$2.5^{+1.6}_{-0.6}$	12^{+7}_{-7}	36^{+14}_{-14}	17 (35)
3405	17^{+14}_{-10}	$6.1^{+0.9}_{-0.7}$	18^{+6}_{-5}	$2.0^{+0.4}_{-0.4}$	53^{+10}_{-10}	307^{+61}_{-61}	33 (32)
3412	44^{+24}_{-15}	$8.2^{+1.4}_{-1.6}$	5^{+2}_{-2}	$2.7^{+0.7}_{-0.4}$	20^{+9}_{-9}	85^{+29}_{-29}	33 (48)
3846	<169	$7.4^{+3.3}_{-2.5}$	5^{+6}_{-3}	$2.2^{+2.9}_{-0.9}$	9^{+5}_{-5}	44^{+20}_{-20}	8 (16)
3847	<59	$5.1^{+3.2}_{-1.2}$	8^{+5}_{-6}	$1.8^{+0.9}_{-0.8}$	7^{+3}_{-3}	32^{+15}_{-15}	4 (16)
3848	35^{+40}_{-20}	$6.5^{+0.8}_{-0.6}$	12^{+3}_{-3}	$2.5^{+0.6}_{-0.5}$	24^{+6}_{-6}	161^{+23}_{-23}	57 (51)
3851	<17	$5.0^{+0.7}_{-0.6}$	19^{+5}_{-5}	$1.3^{+0.7}_{-4.3}$	25^{+18}_{-18}	130^{+77}_{-77}	16 (21)
3852	18^{+60}_{-13}	$6.6^{+0.9}_{-0.81}$	10^{+3}_{-3}	$2.6^{+0.7}_{-0.5}$	18^{+7}_{-7}	$92^{+15.0}_{-15.0}$	44 (47)

Table 15. (Continued.)

Trigger #*	$N_{\rm H}{}^{\dagger}$ ($10^{22}\,{\rm cm}^{-2}$)	$kT_{\rm BB}{}^{\ddagger}$ (keV)	$R_{\rm BB}\left(\frac{d}{15\,{\rm kpc}}\right)^{\S}$ (km)	$\alpha^{\parallel}$	$F_{\rm X}{}^{\#}$	$F_{\gamma}{}^{\#}$	χ^2 (d.o.f.)
3854	51^{+42}_{-26}	$4.4^{+1.7}_{-0.9}$	20^{+13}_{-12}	$2.9^{+1.0}_{-0.6}$	32^{+14}_{-14}	99^{+40}_{-40}	28 (33)
3873	<81	$5.1^{+0.8}_{-0.6}$	19^{+5}_{-8}	$2.0^{+0.8}_{-1.0}$	28^{+9}_{-9}	159^{+43}_{-43}	25 (31)
3874	22^{+20}_{-14}	$5.9^{+0.3}_{-0.2}$	25^{+3}_{-3}	$2.1^{+0.4}_{-0.5}$	56^{+7}_{-7}	408^{+33}_{-33}	36 (50)

* HETE-2 trigger number.
† Photoelectric absorption with 90% confidence level uncertainties.
‡ Blackbody temperature with 90% confidence level uncertainties.
§ Emission radius with 90% confidence level uncertainties, where d is the source distance. We used $d = 15\,{\rm kpc}$.
‖ Spectral index with 90% confidence level uncertainties.
X-ray (2–10 keV) and gamma-ray (10–100 keV) fluxes, $10^{-8}\,{\rm erg\,cm^{-2}\,s^{-1}}$, with 68% confidence level uncertainties.

Table 16. Spectral parameters obtained using BB+PL model for SGR 1900+14.

Trigger #*	$N_{\rm H}{}^{\dagger}$ ($10^{22}\,{\rm cm}^{-2}$)	$kT_{\rm BB}{}^{\ddagger}$ (keV)	$R_{\rm BB}\left(\frac{d}{10\,{\rm kpc}}\right)^{\S}$ (km)	$\alpha^{\parallel}$	$F_{\rm X}{}^{\#}$	$F_{\gamma}{}^{\#}$	χ^2 (d.o.f.)
1568	43^{+77}_{-35}	$7.0^{+1.3}_{-1.3}$	7^{+4}_{-2}	$2.6^{+1.9}_{-1.0}$	26^{+18}_{-18}	157^{+66}_{-66}	20 (24)
1571	15^{+12}_{-8}	$6.6^{+0.3}_{-0.3}$	13^{+2}_{-1}	$2.2^{+0.3}_{-0.2}$	65^{+11}_{-11}	419^{+22}_{-22}	71 (58)
1572	<145	$6.8^{+1.2}_{-1.9}$	6^{+4}_{-3}	$2.1^{+2.9}_{-5.1}$	21^{+18}_{-18}	153^{+99}_{-99}	7 (11)
1578	<48	$6.8^{+0.8}_{-0.7}$	7^{+2}_{-2}	$2.8^{+6.3}_{-1.9}$	24^{+19}_{-19}	112^{+16}_{-16}	5 (11)
2310	<9	$3.7^{+0.6}_{-0.6}$	15^{+5}_{-6}	<2.0	16^{+8}_{-8}	52^{+36}_{-36}	8 (16)

* HETE-2 trigger number.
† Photoelectric absorption with 90% confidence level uncertainties.
‡ Blackbody temperature with 90% confidence level uncertainties.
§ Emission radius with 90% confidence level uncertainties, where d is the source distance. We used $d = 10\,{\rm kpc}$.
‖ Spectral index with 90% confidence level uncertainties.
X-ray (2–10 keV) and gamma-ray (10–100 keV) fluxes, $10^{-8}\,{\rm erg\,cm^{-2}\,s^{-1}}$, with 68% confidence level uncertainties.

July, while INTEGRAL recorded bursts mostly in August, September, and October (Götz et al. 2006).

Many HETE-2 detected bursts in the summer of 2004 when the source was very active. Thus, we investigated the cumulative number–intensity distribution using only the 2004 data. The dot-dashed stepwise line in figure 9 shows the corrected distribution, and the dot-dashed straight line shows a power-law fit, which has a flatter slope of -1.1 ± 0.6. This slope is consistent with those from KONUS and INTEGRAL. This implies that more energetic bursts should occur relatively more frequently in periods of greater activity.

Since the slope for SGR 1806−20 has been reported to be similar to that for SGR 1900+14 (Aptekar et al. 2001), we compared the corrected distribution with the fluence of an intermediate flare from SGR 1900+14 detected by HETE-2. The amounts of observing durations in each year are described in the parentheses of table 2. Concerning the intermediate flare from SGR 1900+14 detected by HETE-2, the amount observing duration was 10450 ks from 2001 to 2005, and therefore the burst rate was 8.3×10^{-3} bursts $\rm d^{-1}$, where the quoted error corresponds to the Poisson error. The 2–100 keV fluence is estimated to be $1.9\times10^{-5}\,{\rm erg\,cm^{-2}}$ using the spectral parameters in Olive et al. (2004). It is shown as a star symbol in figure 9. The fluence of the intermediate flare appears to be fully consistent with the distribution of the short bursts in 2004, at $\sim 10^{-5}\,{\rm erg\,cm^{-2}}$. This could imply a common origin or production mechanism for both short bursts and intermediate flares. Considering the good fit with a single power-law model, it may also imply that there is no characteristic size for the short bursts from SGR 1806−20 up to $F \sim 10^{-5}\,{\rm erg\,cm^{-2}}$.

On the other hand, the fluence of the most energetic giant flare, from SGR 1806−20 on 2004 December 27 is $\sim 2\,{\rm erg\,cm^{-2}}$ for the initial 0.6 s (Terasawa et al. 2005) and the burst rate is 9.8×10^{-5} bursts $\rm d^{-1}$, taking into account the time since the discovery of SGR 1806−20 ($\sim$ 28 years). This is clearly inconsistent with the distribution of the short bursts and the intermediate flare (the difference in the energy bands has little effect). This is consistent with the fact that giant flares are thought to originate from different physical processes.

Although the fluence of the unusual flare from SGR 1900+14 was $\sim 1.9\times10^{-5}\,{\rm erg\,cm^{-2}}$ (Ibrahim et al. 2001), which was the same as the fluence of the intermediate flare from SGR 1900+14, its much longer duration of ~ 1000 s was clearly inconsistent with the duration distribution. This may imply that the taxonomy (i.e., short, intermediate, unusual or giant) is defined by neither the duration nor the fluence.

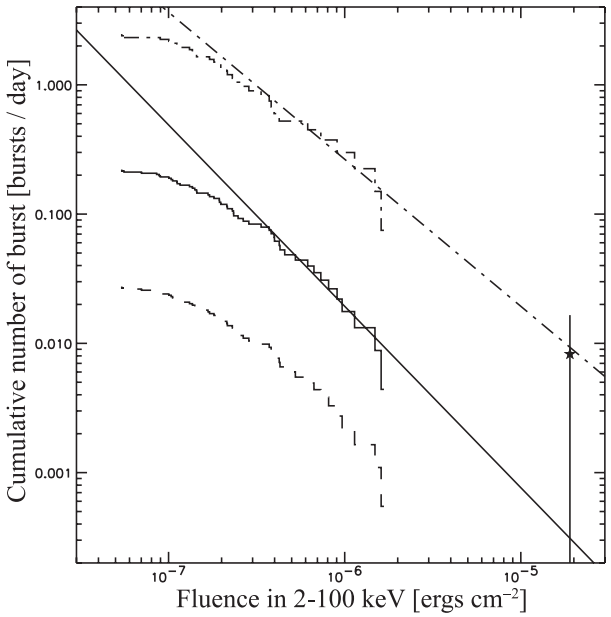

Fig. 9. Cumulative 2–100 keV number–intensity distribution for SGR 1806−20. The dashed line represents the observational data. The solid stepwise line represents the data corrected for the observational efficiency, and the solid straight line represents the fit to it. The dot-dashed stepwise line shows the corrected distribution using the data in 2004 and the dot-dashed straight line shows its fitting result. The star symbol is for the intermediate flare.

The power-law cumulative number–intensity distribution of SGR bursts is similar to that of earthquakes (e.g., Kagan 1999) or solar flares (e.g., Dennis 1985); the former relation is sometimes referred to as the Gutenberg–Richter law. These imply that the SGR bursts could be due to starquakes, or a similar process to solar flares. Considering that the slopes for earthquakes are thought to be influenced by, for example, such as the plate convergence rate (e.g., Kagan 1999), the difference in the slopes for SGR bursts might reflect the intrinsic activities of the SGRs; in other words, starquakes in different zones of a neutron star surface would give different slopes.

4.2. Temporal Properties

Figure 10 shows light curves with 0.5 ms and 5 ms time bins for six bright bursts. These are classified as "single" peaked bursts by the procedure using 5 ms time bin data (see section 2). However, more complex and spiky structures are evident in the light curves with 0.5 ms time bins. Clearly the classification between single- and multiple-peaked bursts is not based only on the intrinsic nature of the bursts, themselves, but is also highly dependent on the time resolution and/or statistics of the observations.

We find a delay of the softer emission compared with that in the 30–100 keV band in short bursts from SGR 1806−20; $T_{\rm lag} = 2.2 \pm 0.4$ ms for 2–10 keV, and $T_{\rm lag} = 1.2 \pm 0.3$ ms for 6–30 keV. Unfortunately the number of bursts is too small to estimate $T_{\rm lag}$ for SGR 1900+14. One possible explanation is rapid spectral softening. Considering that the samples do not show a clear spectral evolution with a 20 ms time resolution, spectral softening with a much faster time scale (a few milliseconds) should be required. The cooling time scale of the emission from the higher blackbody component of 2BB is

$$\tau_{\rm bb} = 0.08 \left(\frac{kT_{\rm HT}}{11\,{\rm keV}}\right)^{4} \left(\frac{R_{\rm HT}}{4.5\,{\rm km}}\right)^{3} \left(\frac{L_{\rm HT}}{10^{40}\,{\rm erg\,s^{-1}}}\right)^{-1} {\rm ms}, \quad (1)$$

where $L_{\rm HT}$ is the luminosity of the emission from the higher blackbody component of 2BB. Assuming that $kT_{\rm HT} \sim 11$ keV, $R_{\rm HT} \sim 4.5$ km, and $L_{\rm HT} \sim 10^{40}\,{\rm erg\,s^{-1}}$, $\tau_{\rm bb}$ turns out to be 0.08 ms, which is much smaller than 20 ms. Therefore, the hypothesis of very rapid spectral softening is plausible. In addition, the time lag, $T_{\rm lag}$, between the 2–5 keV and 5–10 keV time histories is $T_{\rm lag} = 1.2 \pm 0.7$ ms. Although there is not enough statistics, the positive time lag may be due to spectral softening.

An alternative explanation would be the effect of separate emission regions. Figure 11 shows the two spectral components of the 2BB model for #3387. We now evaluate which component dominates, and by how much, in the 2–10 keV, 6–30 keV, and 30–100 keV bands for this burst. The ratios of counts expected from the lower temperature component to counts from the higher temperature component are 5.3, 2.6, and 0.3 for 2–10 keV, 6–30 keV, and 30–100 keV, respectively. Therefore, the 2–10 keV energy range represents the lower temperature component, a nonzero $T_{\rm lag}$ between 2–10 keV and 30–100 keV implies that these two components come from different regions and/or different radiation mechanisms, even though the 2BB model may only be empirical. Thus, the presence of a time lag supports a multiple-component model; at least, the spectra of short bursts consists of a softer and a harder emission component.

It is noteworthy that the small, but clear, time lag for SGR short bursts is different from the large time lags claimed for the long GRBs (e.g., Norris 2002). Furthermore, this is also different from the zero time lag for the short GRBs (e.g., Norris & Bonnell 2006), while the short GRBs remain possible to be generated from SGR giant flares in some scenarios (e.g., Hurley et al. 2005).

We find three bursts (indicated by *d* in table 3) with clear spectral softening, while three short bursts (indicated by *e* in table 3) might have a hard component later in the burst. A possible origin for spectral softening in giant flares is the cooling of a trapped fireball. As we argue in subsection 4.1 and some theoretical works suggest (Duncan & Thompson 1994; Lyutikov 2003), the giant flares are presumably due to different physical processes. And hence, the trapped fireball does not seem to be appropriate for short bursts. Duncan and Thompson (1994) suggested that a small-scale crustal cracking of a neutron star may trigger a short burst. The crustal cracking causes a shift of the magnetic field footpoints. The shift generates Alfvén waves, which accelerate electrons. Considering the short durations of $\sim$ 100 ms of the short bursts, the accelerated electrons do not have to be trapped by a magnetic field, or a fireball. Consequently, the accelerated electrons can simply lose their energies, which may cause the spectral softening. On the other hand, a possible emission mechanism for the hard component could be inverse Compton scattering by a hot plasma located at most a few thousand

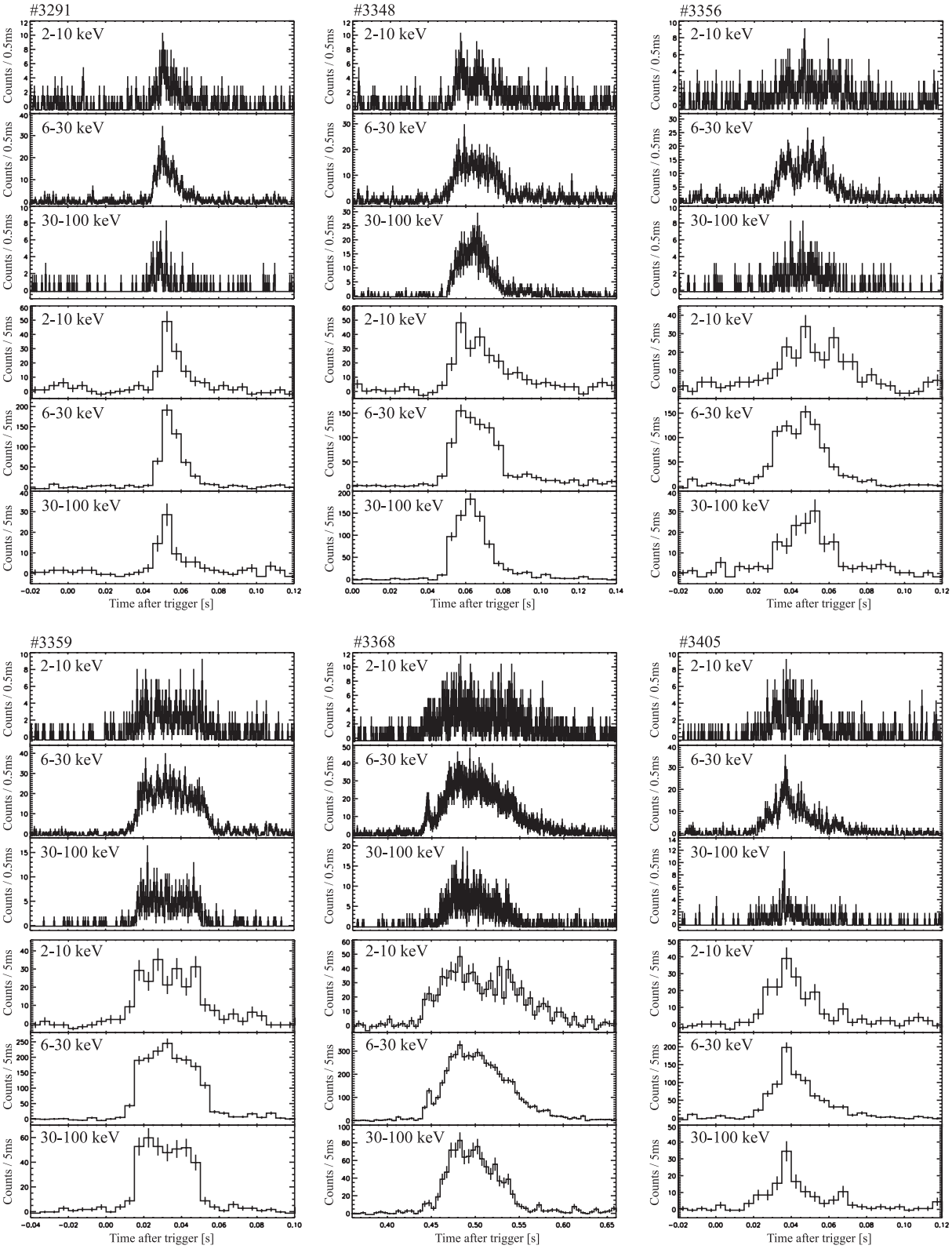

Fig. 10. Examples of the light curves binned with 0.5 ms and 5 ms resolution in various energy bands for the bright single-peaked bursts.

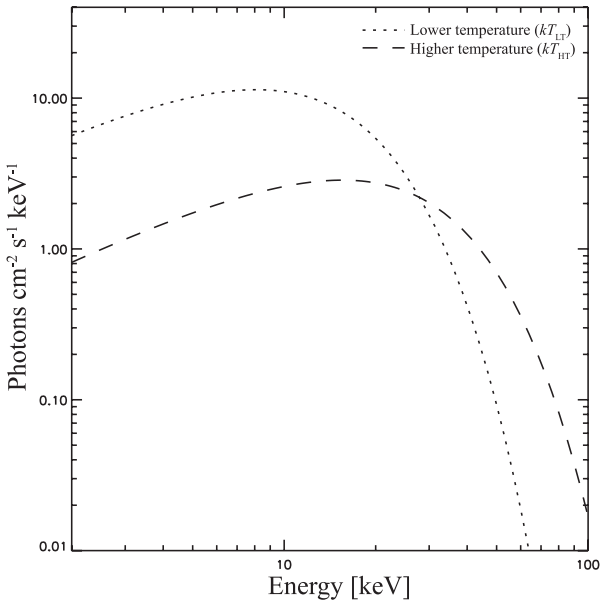

Fig. 11. Comparison of 2BB components for #3387.

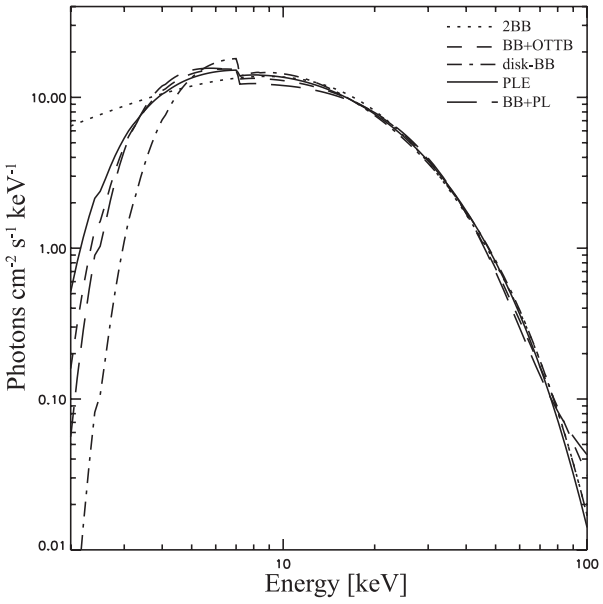

Fig. 12. Comparison of 5 fitting models for #3387.

kilometers away from the SGR (this estimate comes from the duration of the bursts).

A different scenario, proposed by Lyutikov (2003), is that the short bursts are due to heating of the magnetic corona caused by local magnetic reconnections. Moreover, the idea given by Cea (2006) suggests that the glitches in the p-stars cause energy injection into the magnetosphere, which results in bursts.

4.3. Spectral Properties

We tried eight types of spectral models, and found in subsection 3.2 that PLE, BB+OTTB, disk-BB, BB+PL, and 2BB reproduce the observed spectra of the short bursts. Figure 12 compares the spectral shapes of the best-fit models derived for #3387. Since there is no significant difference in their shapes between 5 and 80 keV, high-quality data would be required to distinguish the models in these energy ranges. The current burst data do not have enough statistics to distinguish between them. However, we note that there are signatures of slight excesses in the ranges below 5 keV and/or above 80 keV if PLE, BB+OTTB, disk-BB, and BB+PL are used, while 2BB reproduces all of the spectra in the samples quite well.

From the presence of the time lag, multiple-component models, such as BB+OTTB, BB+PL, and 2BB, are preferred. This could suggest two separate emission regions, a hard-component (30–100 keV) region close to the SGR, and a distant region ($\lesssim$700 km) where the soft component (2–10 keV) could be generated, presumably due to a delayed emission process.

If the SGRs are magnetars, the dominant radiation process in the vicinity of the SGRs should be synchrotron emission. Assuming that X-rays of $\sim$ 10 keV are due to synchrotron emission, the cooling time scale, $\tau_{\rm s}$, is evaluated as

$$\tau_{\rm s} = 3\times10^{-15}\left(\frac{E_{\rm e}}{511\,{\rm keV}}\right)^{-1}\left(\frac{\mu}{5\times10^{32}\,{\rm G\,cm^3}}\right)^{-2}\left(\frac{R}{10^7\,{\rm cm}}\right)^{6}{\rm s}, \quad (2)$$

where $E_{\rm e}$ is the electron energy, μ is the magnetic moment, and R is the distance from the center of the neutron star (Rybicki & Lightman 1979). Even for mildly relativistic electrons at $R \sim 100$ km, $\tau_{\rm s}$ turns out to be just $\sim 3\times10^{-15}$ s under the condition in which the magnetic field $B \sim 5\times10^{14}$ G at the stellar surface. Therefore, in the magnetar model, the power-law type spectra in PLE or BB+PL might be due to synchrotron emission from nonthermal electrons.

For PLE, the peak energy of the νF_ν spectrum, $E_{\rm p}$, is distributed mostly between 15 and 40 keV. Using the analogy of synchrotron shock models for GRBs, $E_{\rm p}$ may be associated with the electron energy distribution. If this is the case, short bursts from SGRs could be related to softer electrons than those required for the hard GRB spectra, whose $E_{\rm p}$ distribution extends into the MeV region. Also, the very strong magnetic field environment might give rise to non-linear magnetic QED effects between photons and the field. Hard emission (over $\sim$ 1 MeV) could be suppressed due to photon splitting, or soft X-rays could be enhanced by the lensing effect due to vacuum polarization (Kohri & Yamada 2002).

The difficulty of this synchrotron-dominated PLE model is in interpreting the possible time lag in the single-component framework, and in explaining the large absorbing matter, necessary to get an acceptable fit, which should be ejected prior to bursts.

In the case of BB+PL, the PL component may be explained as synchrotron emission. Considering the steep PL indices, $\sim$ 2.1, and the BB temperature, $\sim$ 5.5 keV, the soft emission is dominated by the PL component. This appears to be inconsistent with the time lag, which suggests that the soft X-rays are emitted from a distant location. Furthermore, some

unknown radiation process must be invoked to dominate over synchrotron in the hard X-ray band, where the spectral shape can be reproduced by a blackbody function with $kT \sim 5\,\mathrm{keV}$.

Fitting with BB+OTTB gives the best-fit temperatures, $kT_{\mathrm{BB}} \sim 5\,\mathrm{keV}$ and $kT_{\mathrm{OTTB}} \sim 27\,\mathrm{keV}$, and implies that the higher energy emission is due mainly due to the OTTB component. Considering the millisecond variations present in the short bursts, the emission region should have a size of $R \sim 300\,\mathrm{km}$. Therefore, the electron density should be $n_{\mathrm{e}} \lesssim {\sigma_{\mathrm{T}}}^{-1} R^{-1} \sim 5 \times 10^{16}\,\mathrm{cm}^{-3}$ for an optically thin region, where σ_{T} is the Thomson cross section. OTTB is unlikely to be dominant if the SGR is a magnetar because synchrotron emission should be more efficient than bremsstrahlung by many orders of magnitude ($B \sim 10^{15}$ G) for an optically thin plasma with $kT_{\mathrm{e}} \sim 10\,\mathrm{keV}$ and $n_{\mathrm{e}} \sim n_{\mathrm{p}} \sim 10^{16}\,\mathrm{cm}^{-3}$.

The disk-BB model gives acceptable fits for most short bursts with a few exceptions. This model is based on the physical picture of multiple blackbody emission coming from an accretion disk heated by friction. Most galactic X-ray sources with disk-BB spectra are found in binary systems, but there is no evidence of companions for the SGR sources. Alternatively, an accretion disk might be able to form, due to the fallback of ejecta after a supernova explosion (Michel & Dessler 1981; Heger et al. 2003). In any case, bright quiescent emission would be expected from the disk; however, this emission is dim for SGRs (about four orders of magnitude smaller than that of short bursts).

Another possibility is that bursts come from an X-ray heated fallback disk (Perna et al. 2000), which is heated not only by friction, but also by X-rays from the surface of the neutron star. Recently, Wang, Chakrabarty, and Kaplan (2006) discovered such a disk around AXP 4U 0142+614. If a similar disk is present around an SGR source, one would expect optical, infrared, and submillimeter radiation from the irradiated disk, but no significant X-rays. Much more energetic radiation is required to generate the X-ray emission observed in SGR bursts. Lyutikov (2003) proposed the heating of a magnetic corona around the neutron star by local magnetic reconnection as the cause of short bursts. If these high-energy photons heat a disk, disk-BB type emission might be expected. In this case, the inner radius of the irradiated fallback disk, R'_{in} (Perna et al. 2000), would be

$$R'_{\mathrm{in}} = 2.35 \times 10^{-2} \left(\frac{T'_{\mathrm{in}}}{10^4\,\mathrm{eV}}\right)^{-7/3} \left(\frac{f}{0.5}\right)^{2/3} \eta^{-2/3} \times \left(\frac{L_{\mathrm{burst}}}{10^{40}\,\mathrm{erg\,s^{-1}}}\right)^{2/3} \left(\frac{M}{1.4\,M_\odot}\right)^{-2/3} \mathrm{km}, \quad (3)$$

where T'_{in} is the temperature of the inner disk, f is a factor that expresses the uncertainty in the disk structure, η is the efficiency of energy conversion from the irradiated energy to the short burst energy, L_{burst} is the luminosity of the short burst, M is the mass of the neutron star, and $M_\odot$ is the solar mass. Assuming that $T'_{\mathrm{in}} \sim 10\,\mathrm{keV}$, $f \sim 0.5$, $\eta \sim 1$, $L_{\mathrm{burst}} \sim 10^{40}\,\mathrm{erg\,s^{-1}}$, and $M \sim 1.4\,M_\odot$, R'_{in} turns out to be too small to be plausible, 0.024 km. Consequently an X-ray heated fallback disk is unlikely as an origin for the short bursts, and no feasible physical picture emerges from the disk-BB model.

2BB fits represent all of the short burst spectra well. Olive et al. (2004) suggested that a possible explanation of kT_{HT} for the intermediate flare is emission from a trapped fireball. However, it may be difficult to explain the short bursts by emission from a trapped fireball (see subsection 4.2). As mentioned above, the dominant emission process should be synchrotron if a magnetar is the origin. This suggests a possible inconsistency with the thermal emission. The "blackbody spectra" in 2BB could simply be apparent shapes, and 2BB would only be an empirical formula to represent spectra of short bursts.

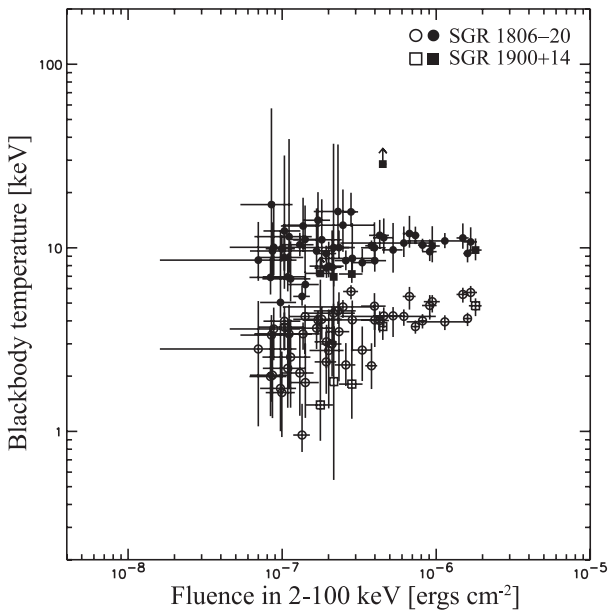

Fig. 13. Relation between the 2–100 keV fluences and blackbody temperatures. The circle and filled circle show kT_{LT} and kT_{HT} respectively for SGR 1806−20. The square and filled square show kT_{LT} and kT_{HT} respectively for SGR 1900+14.

However, it is remarkable that the two blackbody temperatures are found in clearly separated, rather narrow ranges around 4 and 11 keV for all of the bursts from SGR 1806−20 and SGR 1900+14, whose fluences are distributed over nearly two orders of magnitude. Figure 13 shows the 2BB temperatures as a function of the 2–100 keV fluence. These values, ~ 4 and ~ 11 keV, are consistent with those found in previous studies that included much brighter events (Feroci et al. 2004; Olive et al. 2004; Nakagawa et al. 2005; Götz et al. 2006). The temperatures do not seem to depend on either the burst magnitude, the event morphology (i.e., single peaked or multiple peaked) or the source (SGR 1806−20 or SGR 1900+14) (see also Nakagawa et al. 2005).

The (weighted) linear correlation coefficients between the fluence $\log(F)$ and $\log(kT_{\mathrm{LT}})$ or $\log(kT_{\mathrm{HT}})$ are $r_{\mathrm{LT}} = 0.66$ and $r_{\mathrm{HT}} = 0.35$, respectively; kT_{LT} appears to have a slight positive correlation with the fluence, while kT_{HT} does not. The relation between R_{LT} and R_{HT} is shown in figure 14. The dotted lines show that the ratio defined as $C = R_{\mathrm{HT}}^2 / R_{\mathrm{LT}}^2$ obtains a constant value. The line with $C = 0.01$ seems to be consistent with the trend of the data. This relation is theoretically proposed within the framework of the p-stars (Cea

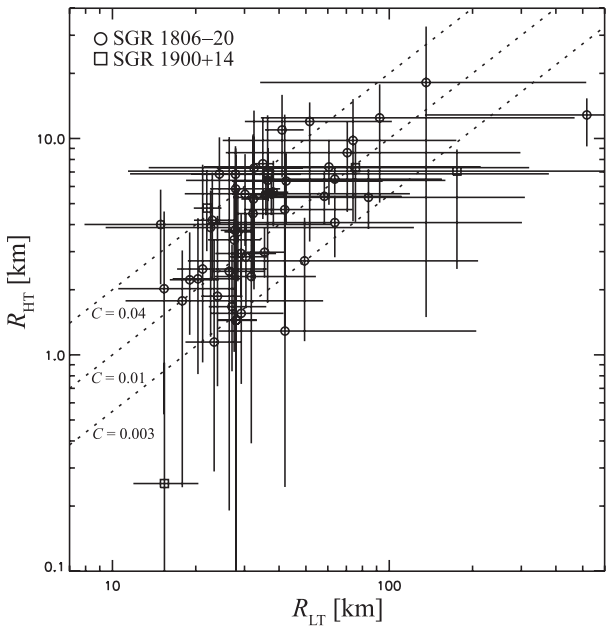

Fig. 14. Relation between the lower temperature blackbody emission radii ($R_{\rm LT}$) and those of the higher temperature blackbody ($R_{\rm HT}$). The dotted lines show that the ratio defined as $C = R_{\rm HT}^2/R_{\rm LT}^2$ get constant value. They have a positive linear correlation with coefficient $r_R = 0.79$.

2006). The (weighted) linear correlation coefficient between $\log(R_{\rm LT})$ and $\log(R_{\rm HT})$ is $r_R = 0.79$. These apparently constant temperatures may imply a unified view of burst mechanisms and/or radiative transfer, for both SGR 1806−20 and SGR 1900+14.

The other notable result is the time lag of the softer radiation with respect to the hard component, $T_{\rm lag} \sim 2.2$ ms (see subsubsection 3.1.2). The softer, $kT_{\rm LT} \sim 4$ keV, component could be reprocessed radiation from the harder, $kT_{\rm HT} \sim 11$ keV, emissions, which might be generated near the SGR site (e.g., in the magnetosphere). If this is the case, the distance to the reprocessing region from the $kT_{\rm HT}$ emitting region is $d_{\rm lag} \lesssim 700$ km, and $R_{\rm LT} \sim 27$ km could represent the size of the reprocessing region (e.g., hot plasma or disk).

According to theoretical studies, a disk with an extremely high density of $\rho(r_{\rm A}) \sim 10^7\,{\rm g\,cm^{-3}}$ is formed around a neutron star by fallback ejecta after a supernova explosion (Colgate 1971; Michel & Dessler 1981; Heger et al. 2003). The fallback disk could be a candidate of the reprocessing region that emitted the softer, $kT_{\rm LT} \sim 4$ keV, emissions, and should be located outside the Alfén radius. Assuming a dipole magnetic field, the Alfvén radius, $r_{\rm A}$, is evaluated as

$$r_{\rm A} = 14 \left(\frac{\mu}{5\times10^{32}\,{\rm G\,cm^3}}\right)^{\frac{2}{5}} \left(\frac{M}{1.4\,M_\odot}\right)^{-\frac{1}{5}} \times \left[\frac{\rho(r_{\rm A})}{10^7\,{\rm g\,cm^{-3}}}\right]^{-\frac{1}{5}} {\rm km}, \quad (4)$$

where μ is the magnetic moment, which could be $\sim 5\times10^{32}\,{\rm G\,cm^3}$, M is the mass of the neutron star, $M_\odot$ is the solar mass, and $\rho(r_{\rm A})$ is the density of the medium. As a result, $r_{\rm A}$ turns out to be 14 km for $M = 1.4M_\odot$, even when the very dense disk is formed, and having a weak dependence on the density, $r_{\rm A} \propto \rho(r_{\rm A})^{-1/5}$. Therefore, the case that $d_{\rm lag} \gtrsim r_{\rm A}$ is plausible, and the reprocessed thermal emission could be generated from the hot plasma or a part of the disk.

For the PLE, BB+PL, BB+OTTB, and disk-BB models, a large absorption ($\sim 10^{23}\,{\rm cm^{-2}}$) is required to achieve acceptable fits. The absorption for the quiescent emission is on the order of $10^{22}\,{\rm cm^{-2}}$, and is therefore inconsistent with the large absorption during the short bursts. Does a cool absorbing medium emerge only with short bursts? It is unlikely that cool matter ejection occurs together with, or shortly before, energetic emission from the source. Fits with 2BB do not require this large absorption column, and 2BB is preferable for this reason, in addition to the presence of a time lag, even though it may be just a convenient empirical form that represents the two-component spectrum.

Based on the discussions for temporal and spectral analyses (see subsections 4.2 and 4.3), two other explanations of the emission mechanism of short bursts should be discussed. The first explanation could be given by very rapid (a few milliseconds) energy reinjection and cooling at the emission region (see subsection 4.2). In this framework, the nonzero time lag would be due to a spectral softening with a time scale of a few milliseconds. The harder component of 2BB would correspond to energy reinjection to the emission region (e.g., plasma in the magnetosphere), while the softer component would correspond to its cooling phase. As the second explanation, spatially diffused plasma trapped in the magnetosphere could be heated and emit radiation; the Alfvén waves due to the starquake, for example, would thermalize the contiguous regions of the plasma from the inside to the outside along the magnetic field lines. The Alfvén velocity becomes very close to the velocity of light near to the surface of magnetars, and the propagating distance of the Alfvén waves in ~ 2.2 ms should be $\lesssim 700$ km. Considering that it should be limited by the distance along the magnetic field lines around the magnetars, the emission radius of the softer component, $R_{\rm LT} \sim 27$ km, is comparable. In this case, the spectral shape should be reproduced by a multiple blackbody model and the 2BB spectra could just mimic its shape.

5. Conclusion

In five years from 2001 to 2005, HETE-2 localized 62 and 6 events from SGR 1806−20 and SGR 1900+14, respectively. Its wide energy range, 2–400 keV, allowed ideal studies of the temporal and spectral properties of these events. Among them, most bursts do not display any clear spectral (hardness) evolution with a rather long time scale of $\gtrsim 20$ ms, with six exceptions, among which three display clear spectral softening and three others might have a hard component at the end.

The data suggest a possible time lag of $T_{\rm lag} \sim 2.2$ ms for the softer radiation (2–10 keV), compared to the harder emission (30–100 keV). One possible explanation could be by a *very rapid* spectral change, softening followed by very rapid re-hardening, with a time scale shorter than a few milliseconds, which were *not observable* by HETE-2 because of the instrumental limit on the time resolution. This requires

an emission mechanism with very rapid ($\lesssim$ a few milliseconds) energy reinjection and cooling at the emitting region, or spatially contiguous heating of the plasma with a nonuniform density in the magnetosphere near magnetars.

Alternatively, the nonzero time lag favors two emission regions. The spectra of all short bursts from SGR 1806−20 and SGR 1900+14 are well fitted by 2BB with $kT_{\rm LT} \sim 4$ keV and $kT_{\rm HT} \sim 11$ keV. Considering the time lag, the X-rays corresponding to the $kT_{\rm HT}$ "blackbody" may be emitted near the SGRs and reprocessed by media located at $d_{\rm lag} \lesssim 700$ km into a softer "blackbody" component with $kT_{\rm LT}$.

The 2–100 keV cumulative number–intensity distribution is represented by a power law with index -1.4 ± 0.4 for all bursts, and -1.1 ± 0.6 for bursts recorded only in 2004. The fluences of the intermediate flare (Olive et al. 2004) and the unusual flare (Ibrahim et al. 2001) from SGR 1900+14 seem to be consistent with the distribution for the 2004 data. This may imply that more energetic bursts occur relatively more frequently in an active phase.

We would like to thank the members of the HETE-2 team for their support. We would like to thank an anonymous referee for comments and suggestions that improved our paper. The HETE-2 mission is supported in the US by NASA contract NASW-4690, in Japan in part by the Ministry of Education, Culture, Sports, Science and Technology Grant-in-Aid 14079102, and in France by CNES contract 793-01-8479. KH is grateful for support under MIT Subcontract MIT-SC-R–293291. YEN is supported by the JSPS Research Fellowships for Young Scientists.

References

Aptekar, R. L., Frederiks, D. D., Golenetskii, S. V, Il'inskii, V. N., Mazets, E. P., Pal'shin, V. D., Butterworth, P. S., & Cline, T. L. 2001, ApJS, 137, 227
Atteia, J.-L. et al. 2003, in AIP Conf. Proc. 662, Gamma-Ray Burst and Afterglow Astronomy, ed. G. R. Ricker & R. K. Vanderspek (Melville: AIP), 17
Cameron, P. B., et al. 2005, Nature, 434, 1112
Cea, P. 2006, A&A, 450, 199
Cline, T., Frederiks, D. D., Golenetskii, S, Hurley, K., Kouveliotou, C., Mazets, M., & Van Paradijs, J. 2000, ApJ, 531, 407
Cline, T. L., et al. 1980, ApJ, 237, L1
Colgate, S. A. 1971, ApJ, 163, 221
Corbel, S., & Eikenberry, S. S. 2004, A&A, 419, 191
Corbel, S., Wallyn, P., Dame, T. M., Durouchoux, P., Mahoney, W. A., Vilhu, O., & Grindlay, J. E. 1997, ApJ, 478, 624
Dennis, B. R. 1985, Sol. Phys., 100, 465
Dickey, J. M., & Lockman, F. J. 1990, ARA&A, 28, 215
Duncan, R. C., & Thompson, C. 1992, ApJ, 392, L9
Duncan, R. C., & Thompson, C. 1994, in AIP Conf. Proc. 307, Gamma-Ray Bursts. Am. Inst. Phys., ed. G. J. Fishman, J. J. Brainerd, & K. Hurley (Melville: AIP), 625
Evans, W. D. et al. 1980, ApJ, 237, L7
Fenimore, E. E., Klebesadel, R. W., & Laros, J. G. 1996, ApJ, 460, 964
Fenimore, E. E., Laros, J. G., & Ulmen, A. 1994, ApJ, 432, 742
Feroci, M., Caliandro, G. A., Massaro, E., Mereghetti, S., & Woods, P. M. 2004, ApJ, 612, 408
Gaensler, B., Slane, P., Gotthelf, E., & Vasisht, G. 2001, ApJ, 559, 963
Göğüş, E., Kouveliotou, C, Woods, P. M., Thompson, C., Duncan, R. C., & Briggs, M. S. 2001, ApJ, 558, 228
Göğüş, E., Woods, P. M., Kouveliotou, C., van Paradijs, J., Briggs, M. S., Duncan, R. C., & Thompson, C. 2000, ApJ, 532, L121
Golenetskii, S. V., Aptekar, R. L., Guryan, Y. A., Il'inskii, V. N., & Mazets, E. P. 1987, Sov. Astron. Lett., 13, 166
Götz, D., et al. 2006, A&A, 445, 313
Götz, D., Mereghetti, S., Mirabel, I. F., & Hurley, K. 2004, A&A, 417, L45
Heger, A., Fryer, C. L., Woosley, S. E., Langer, N., & Hartmann, D. H. 2003, ApJ, 591, 288
Holland, S. T., Barthelmy, S., Beardmore, A., Gehrels, N., Kennea, J., Page, K., Palmer, D., & Rosen, S. 2005, GRB Coord. Netw. Circ., 4034
Hurley, K., et al. 1999, ApJ, 510, L111
Hurley, K., et al. 2005, Nature, 434, 1098
Ibrahim, A. I., et al. 2001, ApJ, 558, 237
Kagan, Y. Y. 1999, Pure Appl. Geophys., 155, 537
Kohri, K., & Yamada, S. 2002, Phys. Rev. D, 65, 043006
Kouveliotou, C., et al. 1987, ApJ, 322, L21
Kouveliotou, C., et al. 1998, Nature, 393, 235
Lamb, D., et al. 2003, GRB Coord. Netw. Circ., 2351
Laros, J. G., Fenimore, E. E., Fikani, M. M., Klebesadel, R. W., & Barat, C. 1986, Nature, 322, 152
Lyutikov, M. 2003, MNRAS, 346, 540
Mazets, E. P., et al. 1981, Ap&SS, 80, 3
Mazets, E. P., Golenetskii, S. V., Il'inskii, V. N., Aptekar, R. L., & Gur'yan, Yu. A. 1979, Nature, 282, 587
McClure-Griffiths, N. M., & Gaensler, B. M. 2005, ApJ, 630, L161
Michel, F. C., & Dessler, A. J. 1981, ApJ, 251, 654
Nakagawa, Y. E., et al. 2005, Nuovo Cimento C, 28, 625
Norris, J. P. 2002, ApJ, 579, 386
Norris, J. P., & Bonnell, J. T. 2006, ApJ, 643, 266
Olive, J.-F., et al. 2004, ApJ, 616, 1148
Paczyński, B. 1992, Acta Astron., 42, 145
Perna, R., Hernquist, L., & Narayan, R. 2000, ApJ, 541, 344
Ricker, G. R., et al. 2003, in AIP Conf. Proc. 662, Gamma-Ray Burst and Afterglow Astronomy, ed. G. R. Ricker & R. Vanderspek (Melville: AIP), 3
Rybicki, G. B., & Lightman, A. P. 1979, Radiative Processes in Astrophysics (New York: John Wiley & Sons, Inc.)
Shirasaki, Y., et al. 2003, PASJ, 55, 1033
Sonobe, T., Murakami, T., Kulkarni, S. R., Aoki, T., & Yoshida, A. 1994, ApJ, 436, L23
Strohmayer, T. E., & Ibrahim, A. 1998, in AIP Conf. Proc. 428, Fourth Huntsville Symp. on Gamma-Ray Bursts, ed. C. A. Meegan, R. D. Preece, & T. M. Koshut (New York: AIP), 947
Terasawa, T., et al. 2005, Nature, 434, 1110
Thompson, C., & Duncan, R. C. 1995, MNRAS, 275, 255
Thompson, C., & Duncan, R. C. 1996, ApJ, 473, 322
Vrba, F. J., Henden, A. A., Luginbuhl, C. B., Guetter, H. H., Hartmann, D. H., & Klose, S. 2000, ApJ, 533 L17
Wang, Z., Chakrabarty, D., & Kaplan, L. 2006, Nature, 440, 772